Received: 17 November 2019 | Revised: 27 July 2020 | Accepted: 1 August 2020

DOI: 10.1002/navi.397

ORIGINAL ARTICLE

WILEY ION

Sensitivity Analysis of Precision Inertial Sensor-based Navigation System (SAPIENS)

Rachit Bhatia | **David Geller**

Mechanical and Aerospace Engineering, Utah State University, Logan, Utah, United States

Correspondence
Rachit Bhatia, Mechanical and Aerospace Engineering, Utah State University.
Email: rachitbhatia@aggiemail.usu.edu

Funding information
International Space Safety Foundation, Grant/Award Number: Graduate Student Fellowship 2017

Abstract

The future of deep space exploration depends upon technological advancement towards improving spacecraft's autonomy and versatility. This study aims to examine the feasibility of autonomous orbit determination using advanced accelerometer measurements. The objective of this research is to ascertain specific sensor requirements to meet pre-defined mission navigation error budgets. Traditional inertial navigation (dead reckoning and external aiding) is not considered. Instead, measurements from pairs of advanced, highly sensitive accelerometers (e.g., cold atom accelerometers) are used onboard to determine gravity field gradients, which are then correlated to onboard gravity maps and used to determine orbital information. Linear Covariance Theory helps to efficiently conduct an error budget analysis of the system. This error budget analysis helps to determine the effect of specific error sources in the sensor measurements, thereby providing information to rank and compare relevant sensor parameters and determine an optimal sensor configuration for a given space mission. The procedure is repeated to evaluate different accelerometer configurations and sensor parameters.

KEYWORDS

advanced accelerometers, autonomous space navigation, gravity gradiometry, inertial navigation, linear covariance analysis, precision sensors

1 | INTRODUCTION

This paper presents significant results from the PhD dissertation on "Revolution in Autonomous Orbital Navigation (RAON)" and attempts to present a case for autonomous space exploration using onboard ultra-precision inertial sensors (Bhatia, 2019).

Sensitivity Analysis of Precision Inertial Sensor-based Navigation System (SAPIENS) is a study to investigate the feasibility and requirements for an autonomous navigation that can potentially apply to all flight regimes. For any space mission, navigation relies primarily on external aids such as the Global Positioning Systems (GPS), the Tracking and Data Relay Satellite (TDRSS), or the Deep Space Network (DSN). These traditional space navigation techniques limit the range of space exploration capability and require specialized communication and ground-based navigation systems to achieve acceptable levels of spaceflight safety. These additional systems not only require precious onboard resources but are also subject to failures that can increase the risk of the Loss of Crew or Loss of Vehicle condition. For next generation space navigation, there is a need to relieve the traditional navigation techniques by implementing the autonomous navigation system onboard and thus reducing the risk level of Loss of Crew or Loss of Vehicle condition.

This study builds upon the preliminary results obtained during the observability analysis of the navigation system with a simpler environment model (Bhatia & Geller, 2017, 2018; Geller & Bhatia, 2018). The aim is to explore the

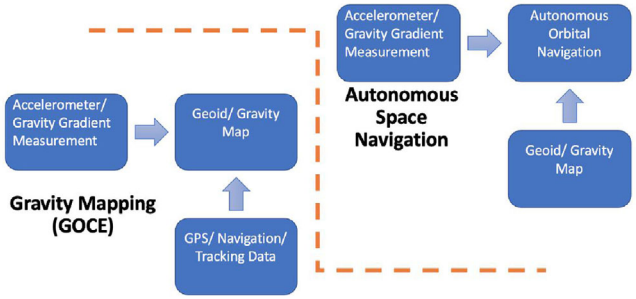

FIGURE 1 Autonomous Space Navigation using Advanced Accelerometer Measurements [Color figure can be viewed in the online issue, which is available at wileyonlinelibrary.com and www.ion.org]

viability of using pairs of advanced accelerometers and onboard gravity field maps to autonomously determine orbital position and velocity for the LEO regime. This study will evaluate the role of advanced accelerometers, used in recent gravity-mapping missions like GRACE-FO (Gravity Recovery and Climate Experiment - Follow On) and GOCE (Gravity Field and Steady-State Ocean Circulation Explorer), in developing and executing autonomous orbital navigation for different sensor and orbit configurations.

Future autonomous orbital navigation architectures need to be suitable and reliable for varying space environments. The navigation approach addressed in this study has the potential to satisfy these requirements. Considering the universal nature of gravity, this approach provides a generic solution for autonomous navigation in almost all types of space environment.

The idea of autonomous space navigation (see Figure 1), as presented in this study, is to reverse the problem of precision gravitational mapping (as achieved during European Space Agency's GOCE mission) and have this high-fidelity gravity map onboard along with a pair of ultra-precise accelerometers. The accelerometer measurements can be correlated to the onboard gravity map to navigate autonomously in the LEO regime.

The objective of this research is to use the Linear Covariance theory to investigate the feasibility and sensor requirements for an autonomous orbit determination using advanced accelerometer measurements and onboard gravity field maps for different sensor and orbit configurations.

2 | GRAVITY GRADIOMETRY/ LITERATURE SURVEY

The study and measurement of the changes in the gravitational acceleration, with respect to the change in spatial position, is termed *gravity gradiometry*. The measurement of gravity gradiometry is a gravity gradient tensor, measured over the given spatial distance.

Hungarian physicist Baron Loránd (Roland) von Eötvös is credited for inventing the first gravity gradiometer instrument in the late 1880s (Király, 1996; Veryaskin, 2018). While working on a series of experiments on the proportionality of inertial and gravitational masses, Eötvös' specialized torsion balance was used to measure the gravitational gradient (Király, 1996). To recognize his ingenious invention, the unit of the gravitational gradient has been named after him (Király, 1996). One Eötvös (E*ö*) is equal to $10^{-9}s^{-2}$ (Gray et al., 1995). The gravity gradient tensor (GGT) is the 3x3 matrix, consisting of nine components of the derivative of the gravitational vector with respect to the position vector.

$$\nabla g = \begin{bmatrix} \nabla g_{XX} & \nabla g_{XY} & \nabla g_{XZ} \\ \nabla g_{YX} & \nabla g_{YY} & \nabla g_{YZ} \\ \nabla g_{ZX} & \nabla g_{ZY} & \nabla g_{ZZ} \end{bmatrix} \tag{1}$$

$$\nabla g_{ij} = \frac{\partial^2 U}{\partial \mathbf{r}_i \partial \mathbf{r}_j}, \; i, j = X, Y, Z, \tag{2}$$

where U is the gravitational potential at the given position vector $\mathbf{r}$. The conservative nature and the continuity of the gravitation field ensures that the gravity gradient matrix is symmetric ($\nabla g_{ij} = \nabla g_{ji}$), and by Laplace's equation, it has zero trace ($\sum_i \nabla g_{ii} = 0$) (Argentiero & Garza-Robles, 1976; Chen et al., 2015; Hofmann-Wellenhof & Moritz, 2006). Thus, only five out of the nine components are independent (Cesare, 2002).

A number of studies have analytically and mathematically decoded the geophysical, gravitational, and spatial information ciphered in the gravity gradient measurements. A publication by Christopher Jekeli on Gravity Gradiometry in 2011 beautifully highlights the rich mathematical foundations of the gravity gradiometry (Jekeli, 2011). He presents the basic mathematical equations leading up to the derivation of gravity gradient tensor and the formulas to compute the minimum and maximum curvature of an equipotential surface, using gravity gradient measurements.

In his paper, Jekeli presents an interesting account of the measurement error analysis of the gravity gradient measurement, specifically the analysis of the required gyroscope and gradiometer noise levels adequate enough to separate the gravity gradient from non-gravitational components.

A more recent effort to extract the positional information of a spacecraft from the gravity gradient matrix includes a paper titled "Gravity Gradient Eigen-Decomposition for Spacecraft Positioning" (2015), by

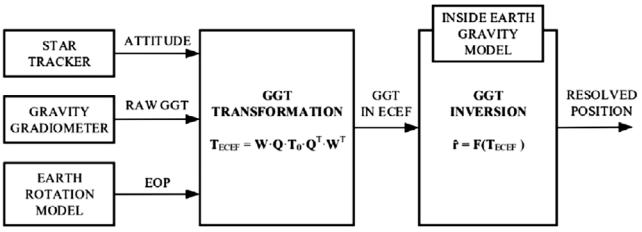

FIGURE 2 Block Diagram of the GGT Inversion Positioning System (Image taken from Chen et al. - "Gravity gradient tensor eigendecomposition for spacecraft positioning" (2015)) (Chen et al., 2015)

Pei Chen, Sun, and Han. In this paper, they comprehensively describe the method to isolate the attitudinal, latitudinal, and longitudinal information from the gravity gradient matrix, assuming that the true gravity field is known (Chen et al., 2015).

Chen and others present an Eigen-Decomposition algorithm for spacecraft positioning using gravity gradient measurements (Figure 2) (Chen et al., 2015). This provides a powerful technique when attitudinal states of the spacecraft are known within permissible limits and a high resolution gravity field model of the primary body is available onboard. Interestingly, this technique does not require any prediction or initial guess. Hence, it is believed that this technique can be significant for dead reckoning and help provide initial guesses for Kalman Filters. To formulate this Eigen-Decomposition algorithm, Chen and others use the J2 spherical harmonics gravity model only. It is believed that this theory can be extended to higher spherical harmonics models or different gravity models as well.

Other attempts made to analytically extract useful information from the gravity gradient matrix include the study titled "Measuring Attitude with Gradiometer" (1994) by David Sonnabend and Thomas G. Gardner (University of Colorado) and the article titled "The gradient tensor of potential field anomalies: Some implications on data collection and data processing of maps" (1990) by Pedersen and Rasmussen (Pedersen & Rasmussen, 1990; Sonnabend & Born, 1994).

A number of publications have extensively highlighted the technical history and mathematical details on the setup and the operating principles of different gravity gradiometers (DiFrancesco et al., 2009a, 2009b; Jekeli, 1993, 2011; Richeson, 2008; Veryaskin, 2018; Wells, 1984). Many other studies have also been found to discuss different approaches and methods for airborne and terrestrial navigation using the GPS integrated gravity gradiometer system (Bobojć & Drożyner, 2003; Paik & Morgan, 1993; Pei et al., 2017; Richeson, 2008; Sun et al., 2016a, 2016b).

Technical details and operating principles of prominent gravity gradiometers have been discussed in detail by Bhatia (Bhatia, 2019). One important point to note here is that an accelerometer rigidly attached to the spacecraft and at a position offset from the center of mass of the system will be able to detect gravity gradient provided the measurement noise level and environment noise is sufficiently low. The results presented in the later sections will convince the reader that the resolution of this gravity gradient measurement improves by adding more accelerometers to the configuration and the performance also depends upon the baseline length, linear distance between the two accelerometers, respectively.

Some studies only discuss terrestrial or airborne navigation, while others only discuss techniques to estimate the spacecraft's position and velocity. Most of the studies consider the integrated inertial navigation system (INS) based on gravity gradient measurements and GPS updates. Most of these studies do not include the objective to compute the required measurement sensitivity to enable the gravity gradiometer based navigation. During the literature survey, no study has been found to discuss the techniques to provide the real-time estimate of the spacecraft's position, velocity, and attitude using gravity gradient measurements only. Further, most of the studies used analytical approaches or Monte Carlo analysis to conduct the measurement error analysis for gravity gradient measurements. No study has been found to analyze the effects of gravity gradiometer measurement sensitivity on the final navigation solution for different sensor and orbit configurations. Thus, as far as the authors know, this research is the first to conduct a Linear Covariance analysis and provide error budgets for gravity gradiometer measurements for different sensor and orbit configurations.

This research offers to complement the existing literature. The contributions include the determination of specific sensor requirements and optimal sensor configuration for different sensor and orbit configurations.

Today, as the technological development of gravity gradiometer instruments enhance their measurement sensitivity, one of the biggest challenges is to isolate the gravity gradient measurements from the disturbing sources (DiFrancesco et al., 2009a, 2009b). This is because with the enhanced measurement sensitivity the resolution of a gravity gradient measurement improves; however, this also improves the resolution of disturbing sources by the same amount (DiFrancesco et al., 2009a, 2009b). Some of the major challenges impacting the full use of gravity gradiometry include the difficulty in obtaining gravity gradient measurements in a dynamic environment, limitations of gradiometer measurement bandwidth for moving-base gravity gradiometers, difficulty in processing gravity gradient measurements and isolating useful measurements

from the disruptive noise sources, and lastly, hardware and data export controls present challenges for the growth of this field (DiFrancesco et al., 2009a, 2009b). It is believed that these challenges can be managed better by understanding the error sources and their contribution towards the system performance, and the error budget analysis provided in this study aims to provide that information.

3 | OBSERVABILITY ANALYSIS

In this section, the results are presented from the study by Geller and Bhatia (2018), where a quantitative standard observability analysis is conducted to demonstrate that three three-axis onboard accelerometer measurements can provide both orbit and attitude observability, i.e., orbital position, velocity, and attitude observability (Geller & Bhatia, 2018). It is assumed that the only forces acting on the spacecraft are due to either a simple point-mass gravity model or the $n \times n$ spherical harmonic gravity model. It is also assumed that the angular velocity and angular acceleration of the spacecraft is known and equal to zero.

The analysis is then extended to show that only two and then only one three-axis accelerometer is required to obtain full-state, position, velocity, and attitude observability under the given assumptions.

The observability metrics used in this analysis are the rank and condition number of the classical observability Gramian. Special care is taken to ensure that the observability Gramian is a well-conditioned matrix.

The observability Gramian is given by

$$\bar{\mathcal{O}}(t_m) \triangleq \sum_{j=1}^{m} \bar{\phi}^T(t_j,t_0)\bar{H}^T(t_j)\bar{H}(t_j)\bar{\phi}(t_j,t_0), \tag{3}$$

where $\bar{H}$ is the measurement partial due to the accelerometer measurements (please refer to Equation (58)), and the state transition matrix $\bar{\phi}(t_j,t_0)$ is computed recursively as

$$\bar{\phi}(t_j,t_0) = \bar{\phi}(t_j,t_{j-1})\bar{\phi}(t_{j-1},t_0), \qquad \bar{\phi}(t_0,t_0) = I_{9\times 9} \tag{4}$$

and where

$$\bar{\phi}(t_j,t_{j-1}) \approx I_{9\times 9} + \bar{F}(t_{j-1})\Delta t + \bar{F}^2(t_{j-1})\Delta t^2/2 + \cdots. \tag{5}$$

In this analysis, the rank and condition number of the observability Gramian in Equation (3) is used as a metric to determine orbit and attitude observability. The analysis looks at two different nominal LEO spacecraft orbits, two different gravity models, and three different accelerometer configurations. In all cases, measurements are taken for 1,500 seconds with a sample rate of one measurement every 30 sec. The nominal vehicle orientation is constant and aligned with the inertial frame. The gravity models are either a point mass gravity model or a 4×4 spherical harmonics model. The LEO orbits have a semi-major axis equal to 7,000 km and an inclination of 56 degrees. The first orbit is circular, and the second orbit has an eccentricity $e = 0.01$.

Observability analysis for the state vector consisting of position, velocity, and attitude shows that even in the best case, the conditions number are on the order of 10^8. This relatively high value leads to the suspicion that the inertial attitude is relatively weakly observable. To confirm this, the above observability analysis was repeated with a state vector consisting of only position and velocity. The attitude was assumed to be known. The results of this observability analysis are shown in Table 1 below.

These results show that position and velocity are strongly observable and confirm the suspicion that attitude is relatively weakly observable (Geller & Bhatia, 2018). Thus, it can be concluded that although it may be theoretically possible to estimate the orbital position, velocity, and attitude using a set of accelerometers, an accurate estimate of attitude may be difficult and require an additional sensor such as a star camera (Geller & Bhatia, 2018).

4 | DYNAMIC MODELS

4.1 | State vector and reference frames

For the given model, the state vector ($\mathbf{x}$) has been defined as follows:

$$\mathbf{x} = \left(\mathbf{x}_s, \mathbf{x}_p, \mathbf{x}_a\right)^T. \tag{6}$$

It consists of 16 spacecraft states ($\mathbf{x}_s$), 3 environmental parameter states ($\mathbf{x}_p$), and 12n (n = number of accelerometers) accelerometer states ($\mathbf{x}_a$), such that

$$\mathbf{x}_s = \left(\mathbf{r}^I_{CM/E}, \mathbf{v}^I_{CM/E}, \mathbf{q}_{I\to B}, \boldsymbol{\omega}^B_{B/I}, \mathbf{r}^B_{CM/O}\right)^T, \tag{7}$$

where $\mathbf{r}^I_{CM/E}$ and $\mathbf{v}^I_{CM/E}$ denote the position and velocity of the spacecraft's center of mass with respect to the center of the Earth, expressed in inertial frame, $\mathbf{q}_{I\to B}$ denote the spacecraft's attitude quaternion, such that it defines the attitude/orientation of the spacecraft body-fixed reference frame with respect to the inertial reference frame, $\boldsymbol{\omega}^B_{B/I}$ is the angular velocity of the spacecraft with respect to the inertial frame, expressed in spacecraft body-fixed frame, and $\mathbf{r}^B_{CM/O}$ denote the spacecraft center of mass position

TABLE 1 Orbit-Only Observability (O)/Unobservability (U) using three three-axis accelerometers and one three-axis accelerometer (Geller & Bhatia, 2018)

		Three 3-axis accelerometers		One 3-axis accelerometer	
		Circular	Elliptical	Circular	Elliptical
Point Mass	Rank	6	6	6	6
	Cond #	110	106	357	345
	U/O	O	O	O	O
4 × 4 Spherical	Rank	6	6	6	6
	Cond #	110	106	359	347
	U/O	O	O	O	O
8 × 8 Spherical	Rank	6	6	6	6
	Cond #	110	106	359	347
	U/O	O	O	O	O

with respect to the origin of the spacecraft body-fixed reference frame.

The three environmental parameter states are given by

$$\mathbf{x}_p = (\beta, \rho_r, h_s)^T, \tag{8}$$

where β is the ballistic coefficient for the spacecraft, ρ_r is the reference sea level atmospheric density, and h_s is the scale height for the exponentially decaying atmospheric drag model.

The accelerometer parameter states are given by

$$\mathbf{x}_a = \left(\mathbf{r}^B_{a_i/O}, \mathbf{b}_i^{\tilde{a}_i}, \mathbf{f}_i^{\tilde{a}_i}, \boldsymbol{\epsilon}_i^{\tilde{a}_i}\right)^T, \tag{9}$$

where $\mathbf{r}^B_{a_i/O}$ denote the i^{th} accelerometer position with respect to the origin of spacecraft body-fixed reference frame, and lastly, $\mathbf{b}_i^{\tilde{a}_i}$, $\mathbf{f}_i^{\tilde{a}_i}$, and $\boldsymbol{\epsilon}_i^{\tilde{a}_i}$ denote the accelerometer bias, scale factor, and misalignment, respectively.

The relevant reference frames (all right-handed and orthogonal) used in this study are the Inertial Reference Frame (IRF), Spacecraft Body-fixed Reference Frame (SBRF), Accelerometer Nominal Reference Frame (ANRF), and Accelerometer Actual Reference Frame (AARF). The first three frames are generally known, while the AARF is generally unknown.

The fundamental inertial reference frame for this study is defined by an origin located at the center of the Earth, x-axis at the intersection of the mean ecliptic plane with the mean equatorial plane at the date of January 1, 2000 and pointing positively towards the vernal equinox, z-axis orthogonal to the mean equatorial plane at the date of January 1, 2000 and y-axis completing a right-handed reference frame.

SBRF is defined as a reference frame, whose center coincides with the nominal center of mass of the spacecraft. The transformation from IRF to SBRF is denoted as $T_{I\to B}$ or $q_{I\to B}$.

ANRF is the accelerometer reference frame, as defined by the manufacturer or as per the accelerometer model. The transformation from SBRF to ANRF is denoted as $T_{B\to a_i^N}$.

AARF is the same as Accelerometer Nominal Reference Frame (ANRF), except that it takes into account the misalignments (ϵ_i) introduced while securing the accelerometer on the spacecraft structure. The transformation from ANRF to AARF is a small angle transformation defined by

$$T_{a_i^N\to\tilde{a}_i} = I_{3\times3} - \left[\epsilon_i^{\tilde{a}_i}\times\right], \tag{10}$$

where $\epsilon_i^{\tilde{a}_i}$ is a vector of three small angle rotations.

4.2 | Environmental models

In this section, relevant environmental models are presented and correspondingly appropriate perturbations acting on the spacecraft are mathematically represented. There are in general two classifications of the perturbations: (1) those that arise from the gravitational potential functions and (2) those that are not derivable from gravitational potential functions (Bond & Allman, 1996). Perturbations like third-body effect (due to the Sun, the Moon, and other massive space objects), gravity gradient torques, or the tidal potential perturbations are classified under the first category as all of these effects can be derived from potential functions (Bond & Allman, 1996). However, perturbations due to atmospheric drag, solar radiation pressure, and other perturbations that involve some "contact" with the spacecraft are classified under the second category (Bond & Allman, 1996).

The spherical harmonics gravity model is used to simulate Earth's gravity model. It is computed analytically by evaluating the first derivative of gravitational potential $U(\mathbf{r})$ with respect to the position vector $\mathbf{r}$.

$$U = \frac{\mu}{r}\left[1 + \sum_{n=1}^{\infty}\sum_{m=0}^{n}\left(\frac{R_E}{r}\right)^n P_{n,m}(s_\lambda)\{C_{n,m}\cos(m\phi) + S_{n,m}\sin(m\phi)\}\right], \tag{11}$$

where gravitational potential $U(\mathbf{r})$ is given by Equation (11), such that μ is the universal gravitational parameter, $\mathbf{r}$ is the position vector from a point O fixed in body E (say Earth) to a generic point Q, r denotes the magnitude of $\mathbf{r}$, R_E is a scaling radius for body E. $P_{n,m}$ is the associated Legendre function of the first kind, of degree n and order m, and has as its argument s_λ, the sine of λ, the latitude of Q (Roithmayr, 1990, 2004). The longitude of Q is denoted by ϕ. $C_{n,m}$ and $S_{n,m}$ are unnormalized gravitational coefficients of degree n and order m (Roithmayr, 1990, 2004). If point O is coincident with the mass center of E, then $C_{1,0}$, $C_{1,1}$, and $S_{1,1}$ all become zero (Roithmayr, 1990, 2004, 2019; Takahashi et al., 2013).

Spacecraft in the lower altitudes (approx. 1,600 km or below) of the low Earth orbit, experience an opposing force or drag due to the interaction with the upper atmosphere. A simplified exponentially decaying atmospheric drag model is used for this study, defined as follows (Gill Oliver & Montenbruck, 2012; Wertz, 1978):

$$\mathbf{a}^I_{aero} = -\frac{1}{2}\rho\left(\mathbf{r}^I_{CM/E}, \rho_r, h_s\right)\beta\left\|\mathbf{v}^I_{CM/E}\right\|\mathbf{v}^I_{CM/E} \tag{12}$$

$$\rho\left(\mathbf{r}^I_{CM/E}, \rho_r, h_s\right) = \rho_r e^{\frac{-\left(\left\|\mathbf{r}^I_{CM/E}\right\| - h_{ref}\right)}{h_s}} \tag{13}$$

$$h_{ref} = 400000 + R_E, \tag{14}$$

where $\mathbf{a}_{aero}$ is the aerodynamic acceleration due to atmospheric drag at spacecraft position $\mathbf{r}^I_{CM/E}$, velocity $\mathbf{v}^I_{CM/E}$, and for ballistic coefficient β, reference atmospheric density ρ_r, and scale height h_s. Further, ρ is the atmospheric density at spacecraft position $\mathbf{r}^I_{CM/E}$, h_{ref} is the reference altitude in meters, at which reference atmospheric density ρ_r and scale height h_s have been defined, and lastly, R_E is the radius of the Earth (Vallado, 2001; Wertz, 1978).

Due to the incident solar radiation, a force is exerted on the spacecraft and this is modeled based on three main factors: (1) the intensity and spectral distribution of the incident radiation, (2) the geometry of the surface and its optical properties, and (3) the orientation of the Sun vector relative to the spacecraft (Wertz, 1978). Here, a simple radiation model is considered, i.e., a constant solar radiation has been assumed (the Earth's albedo and the radiation emitted from the Earth and its atmosphere have been ignored) (Wertz, 1978). The mathematical model of the acceleration due to the solar radiation pressure on a spherical spacecraft can be defined as follows (Wertz, 1978):

$$\mathbf{a}^I_{SRP} = -P_{flux}\left(\frac{3}{r_{sc}\rho_{sc}}\right)\left(\frac{1}{4} + \frac{1}{9}d_r\right)\hat{\mathbf{s}} \tag{15}$$

$$\hat{\mathbf{s}} = -\frac{\mathbf{d}_j}{\left\|\mathbf{d}_j\right\|} = -\frac{\mathbf{r} - \boldsymbol{\rho}_j}{\left\|\mathbf{r} - \boldsymbol{\rho}_j\right\|} = -\frac{\mathbf{r}^I_{CM/E} - \boldsymbol{\rho}_{Sun}}{\left\|\mathbf{r}^I_{CM/E} - \boldsymbol{\rho}_{Sun}\right\|} = \hat{\boldsymbol{\rho}}_{Sun}, \tag{16}$$

where $\mathbf{a}_{SRP}$ is the acceleration due to solar radiation pressure, P_{flux} is the mean momentum flux acting on a surface normal to the Sun's radiation (refer to Equation (17)), r_{sc} is the radius of the spherical spacecraft, ρ_{sc} is the density of the spherical spacecraft, d_r denote the coefficient of diffuse reflection, i.e., the fraction of the incident radiation that is diffusely reflected, $\hat{\mathbf{s}}$ is the unit vector from the spacecraft to the Sun (refer to Equation (16)), $\mathbf{d}_j$ denote the vector from the Sun to the spacecraft, $\mathbf{r}^I_{CM/E}$ is the vector from the Earth to the spacecraft, and $\boldsymbol{\rho}_j$ is the vector from the Earth to the Sun (Wertz, 1978). The mean momentum flux is defined as follows (Wertz, 1978):

$$P_{flux} = \frac{F_e}{c} \tag{17}$$

$$F_e = \frac{1358}{1.0004 + 0.0334\cos D} W/m^2, \tag{18}$$

where F_e is the solar constant (modeled with 1358 W/m^2, i.e., the mean flux at 1 AU, and the denominator is a correction for the true Earth distance), D is the "phase" of the year measured from July 4 (the day of Earth aphelion), and c is the speed of light (Wertz, 1978). It should be noted that the solar constant depends on the radiation wavelength and the eccentricity of the Earth's orbit about the Sun (Wertz, 1978). The variations in this flux (based on the above model) are always less than 0.5%, and solar radiation is largely emitted in the visible and near-infrared portions of the spectrum (Wertz, 1978). For this study, a constant mean momentum flux of $4.4 \times 10^{-6}\, kg \cdot m^{-1} \cdot s^{-2}$ has been considered (see page 130 in reference (Wertz, 1978)).

The perturbing acceleration ($\mathbf{a}^I_{3rd}$), acting on the spacecraft, due to the gravitational force of the massive space objects (Sun and Moon) can be modeled as follows

(Bond & Allman, 1996):

$$\mathbf{a}^I_{3rd} = -Gm_{Sun}\left(\frac{\mathbf{r}^I_{CM/E} - \boldsymbol{\rho}_{Sun}}{\left\|\mathbf{r}^I_{CM/E} - \boldsymbol{\rho}_{Sun}\right\|^3} + \frac{\boldsymbol{\rho}_{Sun}}{\|\boldsymbol{\rho}_{Sun}\|^3}\right)$$

$$-Gm_{Moon}\left(\frac{\mathbf{r}^I_{CM/E} - \boldsymbol{\rho}_{Moon}}{\left\|\mathbf{r}^I_{CM/E} - \boldsymbol{\rho}_{Moon}\right\|^3} + \frac{\boldsymbol{\rho}_{Moon}}{\|\boldsymbol{\rho}_{Moon}\|^3}\right), \quad (19)$$

where m_{Sun} and m_{Moon} are the mass of the Sun and the Moon, and G is the universal gravitational constant.

The gravity gradient torque, due to the point-mass gravitational field of the Earth, acting on the spacecraft is given as follows (Wertz, 1978):

$$\mathbf{M}_{gg} = \frac{3\mu}{\left\|\mathbf{r}^B_{O/E}\right\|^5}\left[\mathbf{r}^B_{O/E} \times \left(J \cdot \mathbf{r}^B_{O/E}\right)\right], \quad (20)$$

where $\mathbf{r}^B_{O/E}$ is the position vector of the spacecraft's geometric center with respect to the center of the Earth, $\mu = GM_E$ is the Earth's gravitational constant, and J is the spacecraft moment-of-inertia tensor (Wertz, 1978). Note that the above expression is valid only if it is assumed that the center of mass of the spacecraft coincides with its geometric center (Wertz, 1978).

4.3 | Nonlinear Dynamics Modeling

The nonlinear dynamics of the spacecraft and the measurements are defined as presented below

The dynamics for the given system can be defined in the general form

$$\dot{\mathbf{x}} = \boldsymbol{f}(\mathbf{x}, t) + G\mathbf{w}, \quad (21)$$

where $\mathbf{x}$ is the true state vector, G is a matrix to map the noise vector to the state dynamics, and $\mathbf{w}$ is a vector of zero-mean white noise processes. The dynamics can then be segmented into three broad categories: (1) translational dynamics, (2) rotational dynamics, and (3) dynamics of the uncertainties inherent to the system/environmental model.

The translational dynamics are defined as

$$\dot{\mathbf{r}}^I_{CM/E} = \mathbf{v}^I_{CM/E} \quad (22)$$

$$\dot{\mathbf{v}}^I_{CM/E} = \mathbf{g}^I_e\left(\mathbf{r}^I_{CM/E}\right) + \mathbf{a}^I_{Third-body}\left(\mathbf{r}^I_{CM/E}, \boldsymbol{\rho}_{Sun}, \boldsymbol{\rho}_{Moon}\right)$$
$$+ \mathbf{a}^I_{aero}\left(\mathbf{r}^I_{CM/E}, \mathbf{v}^I_{CM/E}, \beta, \rho_r, h_s\right)$$
$$+ \mathbf{a}^I_{SRP}\left(\mathbf{r}^I_{CM/E}, \boldsymbol{\rho}_{Sun}\right) + \mathbf{w}_T + \mathbf{w}_{aero}, \quad (23)$$

where $\mathbf{g}_e(\mathbf{r}^I_{CM/E})$ denotes the Earth's gravitational acceleration at position $\mathbf{r}^I_{CM/E}$. In Equation (23), $\mathbf{w}_T$ and $\mathbf{w}_{aero}$ denote the translational disturbance acceleration and unmodeled aerodynamic acceleration, modeled aszero-mean white Gaussian noise. The dynamics for three environmental parameters (β, ρ_r, h_s) are modeled as first-order Markov processes, also known as Exponentially Correlated Random Variables (ECRVs), given as follows:

$$\dot{\mathbf{x}}_p = \frac{\mathbf{x}_p}{\tau_{\mathbf{x}_p}} + \omega_{\mathbf{x}_p}, \quad (24)$$

where $\mathbf{x}_p$ are the parameters, $\tau_{\mathbf{x}_p}$ is the time-constant of the corresponding parameters, and $\omega_{\mathbf{x}_p}$ is the unmodeled zero-mean white Gaussian noise in the dynamics.

The rotational dynamics are defined by the quaternion representing the orientation of the spacecraft body-fixed reference frame (SBRF) with respect to the inertial reference frame (IRF), denoted as $\mathbf{q}_{I\to B}$. The corresponding kinematics and dynamics will be defined as (Markley & Crassidis, 2014)

$$\dot{\mathbf{q}}_{I\to B} = \frac{1}{2}\boldsymbol{\omega}^B_{B/I} \otimes \mathbf{q}_{I\to B}, \quad (25)$$

where $\boldsymbol{\omega}^B_{B/I}$ is the angular velocity of the spacecraft, expressed in the spacecraft-fixed body frame. Correspondingly, the spacecraft's angular acceleration can be defined as (Markley & Crassidis, 2014)

$$\dot{\boldsymbol{\omega}}^B_{B/I} = J^{-1}\left[\mathbf{M}_{gg}\left(\mathbf{r}^I_{CM/E}, \mathbf{q}_{I\to B}\right) - \boldsymbol{\omega}^B_{B/I} \times \left(J\boldsymbol{\omega}^B_{B/I}\right)\right] + \mathbf{w}_R. \quad (26)$$

In Equation (26), $\mathbf{w}_R$ is the rotational disturbance acceleration, modeled as zero-mean white Gaussian noise.

The dynamics of these parameters $(\mathbf{r}^B_{CM/O}, \mathbf{r}^B_{a_i/O}, \mathbf{b}^{\tilde{a}_i}_i, \mathbf{f}^{\tilde{a}_i}_i, \boldsymbol{\epsilon}^{\tilde{a}_i}_i)$ are modeled as ECRVs and generally defined by Equation (24).

4.4 | Linear dynamics modeling

In this section, the aforementioned nonlinear models and equations are linearized about the reference state vector $(\bar{\mathbf{x}})$ so as to formulate the linear covariance model for the given system. Note that for formulating an Extended

Kalman Filter, linearization needs to be done about the estimated state vector ($\hat{\mathbf{x}}$). All the nominal values are decorated with an over-bar.

Also, note that the state vector is "modified" to formulate the linear model (Lefferts et al. 1982). The four-dimensional quaternion state $\mathbf{q}_{I\to B}$ is replaced by the three-dimensional rotation vector $\theta_{I\to B}$ and the quaternion kinematics are replaced by the Bortz equation, given as (Pittelkau, 2003)

$$\dot{\theta} = \omega + \frac{1}{2}\theta\times\omega + \frac{1}{\|\theta\|}\left[1 - \frac{\|\theta\|\sin\|\theta\|}{2(1-\cos\|\theta\|)}\right]\theta\times(\theta\times\omega). \tag{27}$$

Linearization of the rotational dynamics is presented in detail later in this section.

The linearized dynamics of the spacecraft position in inertial frame ($\mathbf{r}^I_{CM/E}$) is given as

$$\delta\dot{\mathbf{r}}^I_{CM/E} = \delta\mathbf{v}^I_{CM/E}. \tag{28}$$

The linearized dynamics of the spacecraft velocity in inertial frame ($\mathbf{v}^I_{CM/E}$) is given as

$$\begin{aligned}\delta\dot{\mathbf{v}}^I_{CM/E} = {} & \left.\frac{\partial\mathbf{g}^I_E\left(\mathbf{r}^I_{CM/E}\right)}{\partial\mathbf{r}^I_{CM/E}}\right|_{\bar{\mathbf{x}}}\delta\mathbf{r}^I_{CM/E} + \left.\frac{\partial\mathbf{a}^I_{3rd}}{\partial\mathbf{r}^I_{CM/E}}\right|_{\bar{\mathbf{x}}}\delta\mathbf{r}^I_{CM/E} \\ & + \left.\frac{\partial\mathbf{a}^I_{aero}}{\partial\mathbf{r}^I_{CM/E}}\right|_{\bar{\mathbf{x}}}\delta\mathbf{r}^I_{CM/E} + \left.\frac{\partial\mathbf{a}^I_{SRP}}{\partial\mathbf{r}^I_{CM/E}}\right|_{\bar{\mathbf{x}}}\delta\mathbf{r}^I_{CM/E} \\ & + \left.\frac{\partial\mathbf{a}^I_{aero}}{\partial\mathbf{v}^I_{CM/E}}\right|_{\bar{\mathbf{x}}}\delta\mathbf{v}^I_{CM/E} + \left.\frac{\partial\mathbf{a}^I_{aero}}{\partial\beta}\right|_{\bar{\mathbf{x}}}\delta\beta \\ & + \left.\frac{\partial\mathbf{a}^I_{aero}}{\partial\rho_r}\right|_{\bar{\mathbf{x}}}\delta\rho_r + \left.\frac{\partial\mathbf{a}^I_{aero}}{\partial h_s}\right|_{\bar{\mathbf{x}}}\delta h_s + \mathbf{w}_T + \mathbf{w}_{aero},\end{aligned} \tag{29}$$

where the partial derivatives in Equation (29) are given in the Appendix, respectively.

The dynamics of the ballistic coefficient, reference atmospheric density, and scale height are already linear.

The linearized rotational kinematics can be described by (Pittelkau, 2003)

$$\delta\dot{\theta} = \delta\omega^B_{B/I} - \bar{\omega}^B_{B/I}\times\delta\theta. \tag{30}$$

The linearized dynamics of the spacecraft's angular velocity ($\boldsymbol{\omega}^B_{B/I}$) are given as (Markley & Crassidis, 2014)

$$\begin{aligned}\delta\dot{\omega}^B_{B/I} = J^{-1}\Bigg[& \left.\frac{\partial M_{gg}}{\partial\mathbf{r}^I_{CM/E}}\right|_{\bar{\mathbf{x}}}\delta\mathbf{r}^I_{CM/E} + \left.\frac{\partial M_{gg}}{\partial\theta}\right|_{\bar{\mathbf{x}}}\delta\theta \\ & - \left.\frac{\partial\left(\omega^B_{B/I}\times\left[J\omega^B_{B/I}\right]\right)}{\partial\omega^B_{B/I}}\right|_{\bar{\mathbf{x}}}\delta\omega^B_{B/I}\Bigg] + \mathbf{w}_R,\end{aligned} \tag{31}$$

where

$$\left.\frac{\partial\left(\omega^B_{B/I}\times\left(J\omega^B_{B/I}\right)\right)}{\partial\omega^B_{B/I}}\right|_{\bar{\mathbf{x}}} = -\left[\left(J\bar{\omega}^B_{B/I}\right)\times\right] + \left[\bar{\omega}^B_{B/I}\times\right]J. \tag{32}$$

The partial derivatives of the gravity gradient torque with respect to the spacecraft position vector and the rotation vector are given in the Appendix, respectively.

The dynamics of the center of mass position with respect to the spacecraft body-fixed frame ($\mathbf{r}^B_{CM/O}$), i^{th} accelerometer position with respect to the spacecraft body-fixed frame ($\delta\mathbf{r}^B_{a_i/O}$), accelerometer bias ($\mathbf{b}_i^{\tilde{a}_i}$), accelerometer scale factor ($\mathbf{f}_i^{\tilde{a}_i}$), and accelerometer misalignment ($\boldsymbol{\epsilon}_i^{\tilde{a}_i}$) are already linear.

5 | ACCELEROMETER MEASUREMENT MODEL

5.1 | Nonlinear measurement modeling

The accelerometer measurements for a system can be generically defined as

$$\tilde{a}_i^{\tilde{a}_i} = \boldsymbol{h}(\mathbf{x}) + \boldsymbol{\eta}_i^{\tilde{a}_i}, \tag{33}$$

where $\mathbf{x}$ is the true state vector, $\boldsymbol{h}(\cdot)$ is a nonlinear function which maps state vector to the accelerometer measurements, and $\boldsymbol{\eta}_i^{\tilde{a}_i}$ is a vector of zero-mean white Gaussian noise on the accelerometer measurements. In this document, the subscript i represents the quantities/vectors related to the i^{th} accelerometer, and the superscript I, B, and $\tilde{a}_i$ denote the vectors coordinatized in the inertial reference frame (IRF), spacecraft body-fixed reference frame (SBRF), and accelerometer actual reference frame (AARF), respectively.

According to Figure 3, the position of the i^{th} accelerometer, with respect to the center of the Earth, can be defined

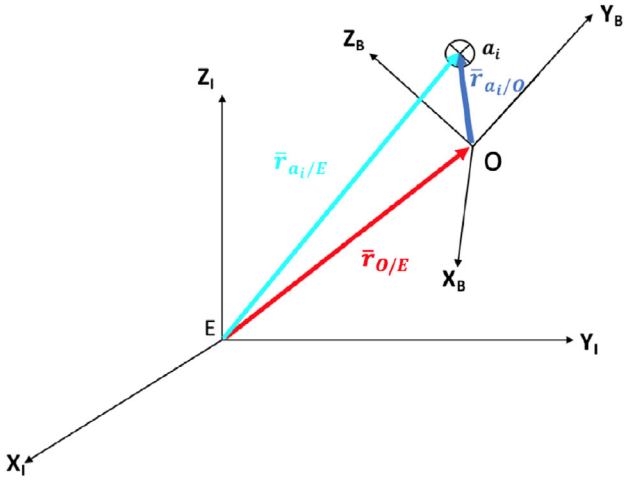

FIGURE 3 Spacecraft's center of mass position vector relative to inertial reference frame (IRF) and spacecraft body-fixed reference frame (SBRF) [Color figure can be viewed in the online issue, which is available at wileyonlinelibrary.com and www.ion.org]

as follows:

$$\mathbf{r}_{a_i/E} = \mathbf{r}_{O/E} + \mathbf{r}_{a_i/O}, \tag{34}$$

where $\mathbf{r}_{a_i/E}$ is the position of the i^{th} accelerometer with respect to the center of the Earth, $\mathbf{r}_{O/E}$ is the position of the origin of the spacecraft body-fixed reference frame with respect to the center of the Earth, and $\mathbf{r}_{a_i/O}$ is the position of the i^{th} accelerometer with respect to the origin of the spacecraft body-fixed reference frame.

Further, it is assumed that the origin O of the spacecraft body-fixed reference frame is fixed to the spacecraft's center of mass CM. However, during Linear Covariance simulation setup, in Section 6.1, an additional state ($\mathbf{r}^B_{CM/O}$) is added to take into account the uncertainty in the estimate of the position of the center of mass with respect to the origin O of the SBRF.

An electrostatic accelerometer is designed to detect the difference between the acceleration of the center of mass of the spacecraft and that of the proof mass of the i^{th} accelerometer by measuring the electrostatic force required to keep the proof mass in the center of the accelerometer. The acceleration of the proof mass $\mathbf{a}^I_{p_i}$ of the i^{th} accelerometer, expressed in the inertial reference frame, can be given as

$$\mathbf{a}^I_{p_i} = \ddot{\mathbf{r}}^I_{a_i/E} = \ddot{\mathbf{r}}^I_{CM/E} + \left(\ddot{\mathbf{r}}^I_{a_i/CM}\right)_{rel} + 2\boldsymbol{\omega}^I_{B/I} \times \left(\dot{\mathbf{r}}^I_{a_i/CM}\right)_{rel} + \dot{\boldsymbol{\omega}}^I_{B/I} \times \mathbf{r}^I_{a_i/CM} + \boldsymbol{\omega}^I_{B/I} \times \left(\boldsymbol{\omega}^I_{B/I} \times \mathbf{r}^I_{a_i/CM}\right), \tag{35}$$

where $\mathbf{a}^I_{p_i}$ is the acceleration of the i^{th} accelerometer's proof mass, $\ddot{\mathbf{r}}^I_{CM/E}$ is the acceleration of the spacecraft, $\left(\ddot{\mathbf{r}}^I_{a_i/CM}\right)_{rel}$ is the acceleration of the i^{th} accelerometer's proof mass with respect to the spacecraft, as viewed relative to the rotating spacecraft body-fixed reference frame, $\left(\dot{\mathbf{r}}^I_{a_i/CM}\right)_{rel}$ denotes the velocity of the i^{th} accelerometer's proof mass with respect to the spacecraft, as viewed relative to the rotating spacecraft body-fixed reference frame, and $\mathbf{r}^I_{a_i/CM}$ is the position of the i^{th} accelerometer's proof mass with respect to the spacecraft.

Using Newton's second law,

$$\mathbf{F}^I_{\upsilon} = m_{\upsilon}\ddot{\mathbf{r}}^I_{CM/E} \tag{36}$$

$$\mathbf{F}^I_{p_i} = m_{p_i}\mathbf{a}^I_{p_i}, \tag{37}$$

where $\mathbf{F}^I_{\upsilon}$ is the total force acting on the spacecraft, m_{υ} is the mass of the spacecraft, $\mathbf{F}^I_{p_i}$ is the total force acting on the i^{th} accelerometer's proof mass, and m_{p_i} is the mass of the i^{th} accelerometer's proof mass.

Force analysis of the i^{th} accelerometer's proof mass yields

$$\mathbf{F}_{p_i} = \mathbf{F}_{g_{p_i}} + \mathbf{F}_{emf_i}, \tag{38}$$

where $\mathbf{F}_{g_{p_i}}$ is the force acting on the i^{th} accelerometer's proof mass due to gravitational field, and $\mathbf{F}_{emf_i}$ is the electro-motive force acting on the i^{th} accelerometer's proof mass to keep the proof mass at the center of the accelerometer frame.

Force analysis of the vehicle yields

$$\mathbf{F}_{\upsilon} = \mathbf{F}_{g_{\upsilon}} + \mathbf{N} - \mathbf{F}_{emf_i}, \tag{39}$$

where $\mathbf{F}_{g_{\upsilon}}$ is the force acting on the spacecraft due to gravitational field, $\mathbf{N}$ is the force acting on the spacecraft due to non-gravitational forces, like atmospheric drag, and $\mathbf{F}_{emf_i}$ is the equal and opposite electro-motive force acting on the spacecraft.

Using free body analysis of the vehicle and i^{th} accelerometer's proof mass, the acceleration of the spacecraft and the acceleration of the i^{th} accelerometer's proof mass can be expressed as below

$$\mathbf{a}^I_{\upsilon} = \mathbf{g}^I\left(\mathbf{r}^I_{CM/E}\right) + \frac{\mathbf{N}^I\left(\mathbf{r}^I_{CM/E}, \mathbf{v}^I_{CM/E}, \beta, \rho_r, h_s\right)}{m_{\upsilon}} - \frac{\mathbf{F}^I_{emf_i}}{m_{\upsilon}} \tag{40}$$

$$\mathbf{a}^I_{p_i} = \mathbf{g}^I\left(\mathbf{r}^I_{CM/E} + \mathbf{r}^I_{a_i/CM}\right) + \frac{\mathbf{F}^I_{emf_i}}{m_{p_i}}. \tag{41}$$

Further,

$$\mathbf{r}^I_{CM/E} + \mathbf{r}^I_{a_i/CM} = \mathbf{r}^I_{a_i/E}, \tag{42}$$

where $\mathbf{r}^I_{a_i/E}$ is the inertial position of the i^{th} accelerometer's proof mass.

The difference between the acceleration of the center of mass of the spacecraft and that of the proof mass of the i^{th} accelerometer is defined as the detected acceleration and is denoted by $\mathbf{a}^I_{d_i}$. The detected acceleration is equal to the sum of all non-gravitational accelerations acting on the proof mass. Thus, using Equation (41) and Equation (42), the detected acceleration is given as

$$\mathbf{a}^I_{d_i} = \frac{\mathbf{F}^I_{emf_i}}{m_{p_i}} = \mathbf{a}^I_{p_i} - \mathbf{g}^I\left(\mathbf{r}^I_{a_i/E}\right). \tag{43}$$

To re-state this rigorously, Equations (40)–(42) are substituted in Equation (35), and it is noted that the detected acceleration measurement is proportional to $\mathbf{F}^I_{emf_i}(\frac{1}{m_{p_i}} + \frac{1}{m_v})$.

Since quantities like position, velocity, and acceleration of the i^{th} accelerometer's proof mass and the spacecraft angular velocity are traditionally measured in the spacecraft body-fixed reference frame (SBRF), these terms are transformed using a transformation matrix from SBRF to IRF. The detected acceleration is then given as

$$\begin{aligned}\mathbf{a}^I_{d_i} = {} & \mathbf{F}^I_{emf_i}\left(\frac{1}{m_{p_i}} + \frac{1}{m_v}\right) = \mathbf{g}^I\left(\mathbf{r}^I_{CM/E}\right) - \mathbf{g}^I\left(\mathbf{r}^I_{a_i/E}\right) \\ & + \mathbf{N}^I\left(\mathbf{r}^I_{CM/E}, \mathbf{v}^I_{CM/E}, \beta, \rho_r, h_s\right) \\ & + T_{B\to I}\left[\boldsymbol{\omega}^B_{B/I} \times \left(\boldsymbol{\omega}^B_{B/I} \times \mathbf{r}^B_{a_i/CM}\right)\right] \\ & + T_{B\to I}\left[\dot{\boldsymbol{\omega}}^B_{B/I} \times \mathbf{r}^B_{a_i/CM}\right] \\ & + 2T_{B\to I}\left[\boldsymbol{\omega}^B_{B/I} \times \dot{\mathbf{r}}^B_{a_i/CM}\right] + T_{B\to I}\left[\ddot{\mathbf{r}}^B_{a_i/CM}\right].\end{aligned} \tag{44}$$

For this measurement model, Equation (33) is expanded, and the accelerometer measurements are given by the detected acceleration in the accelerometer frame $\mathbf{a}^{\tilde{a}_i}_{d_i}$ plus errors due to bias and noise

$$\tilde{a}^{\tilde{a}_i}_i = \mathbf{a}^{\tilde{a}_i}_{d_i} + \mathbf{b}^{\tilde{a}_i}_i + \boldsymbol{\eta}^{\tilde{a}_i}_i, \tag{45}$$

where $\boldsymbol{\eta}^{\tilde{a}_i}_i$ is the accelerometer measurement noise modeled as zero-mean white Gaussian noise with a strength denoted by Q_{η_i}, such that

$$E[\boldsymbol{\eta}^{\tilde{a}_i}_i(t)\boldsymbol{\eta}^{\tilde{a}_i}_i(t')^T] = Q_{\eta_i}\delta(t - t'). \tag{46}$$

This means that if the accelerometer measurement noise resolution is $\boldsymbol{\eta}^{\tilde{a}_i}_i$ $(\frac{m}{s^2\sqrt{Hz}})$, then the power spectral density of the accelerometer noise can be defined as Q_{η_i} $(\frac{m^2}{s^4 Hz}$ or $\frac{m^2}{s^3 2\pi rad})$.

Thus, the measurement covariance R $(\frac{m^2}{s^4 2\pi rad})$ is given as

$$R = \frac{Q_{\eta_i}}{\delta t_{meas}}, \tag{47}$$

where δt_{meas} is the measurement update time in seconds. All vectors with superscript $\tilde{a}_i$ are coordinatized in the actual i^{th} accelerometer frame. In Equation (45), $\mathbf{a}^{\tilde{a}_i}_{d_i}$ denotes the detected acceleration in the accelerometer frame, defined as

$$\mathbf{a}^{\tilde{a}_i}_{d_i} = \left[I + D\left(\mathbf{f}^{\tilde{a}_i}_i\right)\right] T_{a^N_i\to\tilde{a}_i} T_{B\to a^N_i} T_{I\to B}\left[\mathbf{a}^I_{d_i}\right], \tag{48}$$

where $D(\mathbf{f}^{\tilde{a}_i}_i)$ denotes the matrix with accelerometer measurement scale-factors on the diagonal. All vectors with superscript a^N_i are coordinatized in the nominal i^{th} accelerometer frame. The nominal i^{th} accelerometer frame and the actual i^{th} accelerometer frame are different because of the inherent misalignments that occur while setting up the accelerometer in the spacecraft frame. These accelerometer misalignments $(\boldsymbol{\epsilon}^{\tilde{a}_i}_i)$ are accounted for by defining the following small angle rotation:

$$T_{a^N_i\to\tilde{a}_i} = I - \left[\boldsymbol{\epsilon}^{\tilde{a}_i}_i \times\right]. \tag{49}$$

It can be noted that with reasonable assumptions of nearly constant spacecraft angular velocity and a rigid body spacecraft with accelerometers firmly fixed to the spacecraft structure, the last three terms in Equation (44) are very small and can be absorbed into the bias and noise terms in Equation (45).

Further, using vector algebra (refer to Figure 4), the relationship between accelerometer position $(\mathbf{r}^I_{a_i/E})$ with respect to the center of the Earth, expressed in inertial frame, and accelerometer position $(\mathbf{r}^B_{a_i/CM})$ with respect to the spacecraft center of mass, expressed in spacecraft fixed body frame, can be written as

$$\mathbf{r}^I_{a_i/E} = \mathbf{r}^I_{CM/E} + T^T_{I\to B}\left[\mathbf{r}^B_{a_i/CM}\right], \tag{50}$$

where accelerometer position $(\mathbf{r}^B_{a_i/CM})$ with respect to the spacecraft center of mass, expressed in spacecraft fixed body frame, is given as

$$\mathbf{r}^B_{a_i/CM} = \mathbf{r}^B_{a_i/O} - \mathbf{r}^B_{CM/O}. \tag{51}$$

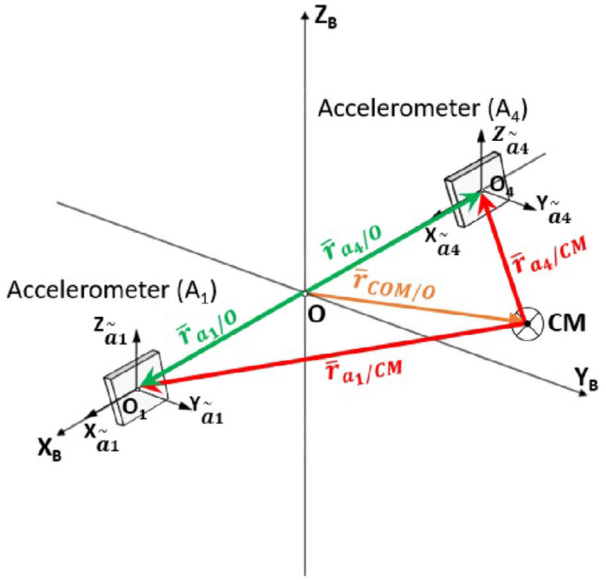

FIGURE 4 Schematic Model (only two of the six accelerometers are shown) (Cesare, 2002) [Color figure can be viewed in the online issue, which is available at wileyonlinelibrary.com and www.ion.org]

Now using Equation (49) in Equation (48), gives

$$\mathbf{a}_{d_i}^{\tilde{a}_i} = \left[I + D\left(\mathbf{f}_i^{\tilde{a}_i}\right)\right]\left(I - \left[\boldsymbol{\epsilon}_i^{\tilde{a}_i}\times\right]\right)T_{B\to a_i^N}T_{I\to B}\left[\mathbf{a}_{d_i}^I\right], \quad (52)$$

where the detected acceleration ($\mathbf{a}_{d_i}^I$), in the inertial frame, can be rewritten using Equations (50)-(51) and ignoring the linear acceleration ($\dot{\bar{\boldsymbol{\omega}}}_{B/I}^B \times \bar{\mathbf{r}}_{a_i/CM}^B$), Coriolis acceleration ($2\bar{\boldsymbol{\omega}}_{B/I}^B \times \dot{\bar{\mathbf{r}}}_{a_i/CM}^B$), and acceleration with respect to the spacecraft ($\ddot{\bar{r}}_{a_i/CM}^B$)

$$\begin{aligned}\mathbf{a}_{d_i}^I = {} & \mathbf{g}^I\left(\mathbf{r}_{CM/E}^I\right) - \mathbf{g}^I\left(\mathbf{r}_{CM/E}^I + T_{B\to I}\left[\mathbf{r}_{a_i/O}^B - \mathbf{r}_{CM/O}^B\right]\right) \\ & + \mathbf{a}_{aero}^I\left(\mathbf{r}_{CM/E}^I, \mathbf{v}_{CM/E}^I, \beta, \rho_r, h_s\right) \\ & + \mathbf{a}_{SRP}^I\left(\mathbf{r}_{CM/E}^I, \boldsymbol{\rho}_{Sun}\right) \\ & + T_{B\to I}\left\{\boldsymbol{\omega}_{B/I}^B \times \left(\boldsymbol{\omega}_{B/I}^B \times \left[\mathbf{r}_{a_i/O}^B - \mathbf{r}_{CM/O}^B\right]\right)\right\}. \quad (53)\end{aligned}$$

This provides the necessary relationship between the measurement $\tilde{a}_i$ and the state $\mathbf{x}$. As noted earlier, an accelerometer rigidly attached to the spacecraft and at a position offset from the center of mass of the system will be able to detect gravity gradient provided the measurement noise level and environment noise is sufficiently low. The term related to the gravity gradient measurement can be noted in Equation (53).

Measurements from an onboard star camera are used to improve the estimation of the states and thereby enhance the overall fidelity of the navigation system. The star camera measurements $\tilde{s}$ are generically defined as

$$\tilde{s}^{\tilde{s}} = \boldsymbol{l}(\mathbf{x}) + \boldsymbol{\eta}_{sc}^{\tilde{s}}, \quad (54)$$

where superscript $\tilde{s}$ denotes the vectors coordinatized in the actual star-camera reference frame (ASRF), $\mathbf{x}$ is the true state vector, $\boldsymbol{l}(\cdot)$ is a nonlinear function which maps state vector to the star camera measurements, and $\boldsymbol{\eta}_{sc}^{\tilde{s}}$ is a vector of zero-mean white Gaussian noise on the star camera measurements with the covariance of the noise denoted by $Q_{\eta_{sc}}(rad^2)$, such that

$$E[\boldsymbol{\eta}_{sc,i}^{\tilde{s}}\boldsymbol{\eta}_{sc,j}^{\tilde{s}\,T}] = Q_{\eta_{sc}}\delta_{ij}, \quad (55)$$

where δ_{ij} is a Kronecker delta function.

The star camera measurements $\tilde{s}$ are modeled as

$$\tilde{s}^{\tilde{s}} = T_{B\to\tilde{s}}\boldsymbol{\theta}_{I\to B} + \boldsymbol{\eta}_{sc}^{\tilde{s}}, \quad (56)$$

where $T_{B\to\tilde{s}}$ is the transformation matrix from the spacecraft body-fixed reference frame (SBRF) to the actual star-camera reference frame (ASRF) and $\boldsymbol{\theta}_{I\to B}$ is the true orientation of the spacecraft body-fixed reference frame (SBRF) with respect to the inertial reference frame (IRF).

For this study, the actual star-camera reference frame (ASRF) is aligned with the spacecraft body-fixed reference frame (SBRF). This means that the misalignments in the setting up of the star camera on the rigid body of the spacecraft have been ignored. Thus, $T_{B\to\tilde{s}}$ is a 3×3 identity matrix.

5.2 | Linearized measurement equation

Now, Equation (33) is linearized as

$$\delta\tilde{a}_i^{\tilde{a}_i} = H_x\delta\mathbf{x} + \boldsymbol{\eta}_i^{\tilde{a}_i}, \quad (57)$$

where H_x is the measurement partial due to the accelerometer measurements, defined as

$$H_x = \left.\frac{\partial\mathbf{h}}{\partial\mathbf{x}}\right|_{\bar{\mathbf{x}}} \quad (58)$$

$$\begin{aligned}H_x = \Bigg[& \left.\frac{\partial\boldsymbol{h}_{3n}}{\partial\mathbf{r}_{CM/E}^I}\right|_{\bar{\mathbf{x}}} \quad \left.\frac{\partial\boldsymbol{h}_{3n}}{\partial\mathbf{v}_{CM/E}^I}\right|_{\bar{\mathbf{x}}} \quad \left.\frac{\partial\boldsymbol{h}_{3n}}{\partial\boldsymbol{\theta}_{I\to B}}\right|_{\bar{\mathbf{x}}} \quad \left.\frac{\partial\boldsymbol{h}_{3n}}{\partial\boldsymbol{\omega}_{B/I}^B}\right|_{\bar{\mathbf{x}}} \\ & \left.\frac{\partial\boldsymbol{h}_{3n}}{\partial\mathbf{r}_{CM/O}^B}\right|_{\bar{\mathbf{x}}} \quad \left.\frac{\partial\boldsymbol{h}_{3n}}{\partial\beta}\right|_{\bar{\mathbf{x}}} \quad \left.\frac{\partial\boldsymbol{h}_{3n}}{\partial\rho_r}\right|_{\bar{\mathbf{x}}} \quad \left.\frac{\partial\boldsymbol{h}_{3n}}{\partial h_s}\right|_{\bar{\mathbf{x}}} \quad \left.\frac{\partial\boldsymbol{h}_{3n}}{\partial\mathbf{r}_{a_i/O}^B}\right|_{\bar{\mathbf{x}}} \\ & \left.\frac{\partial\boldsymbol{h}_{3n}}{\partial\mathbf{b}_i^{\tilde{a}_i}}\right|_{\bar{\mathbf{x}}} \quad \left.\frac{\partial\boldsymbol{h}_{3n}}{\partial\mathbf{f}_i^{\tilde{a}_i}}\right|_{\bar{\mathbf{x}}} \quad \left.\frac{\partial\boldsymbol{h}_{3n}}{\partial\boldsymbol{\epsilon}_i^{\tilde{a}_i}}\right|_{\bar{\mathbf{x}}}\Bigg]_{3n\times(18+12n)}. \quad (59)\end{aligned}$$

Noting that the total number of states is $18+12n$ (where n is the number of accelerometers), the measurement partial H_x is a matrix of dimension size $3n \times (18+12n)$. Measurement partials with respect to each state are given below.

Measurement partials with respect to the spacecraft position in the inertial frame ($\mathbf{r}^I_{CM/E}$) are given as

$$\left.\frac{\partial \boldsymbol{h}}{\partial \mathbf{r}^I_{CM/E}}\right|_{\bar{\mathbf{x}}} = T_{B\to a_i^N} T_{I\to B} \left.\frac{\partial \mathbf{a}^I_{d_i}}{\partial \mathbf{r}^I_{CM/E}}\right|_{\bar{\mathbf{x}}}, \tag{60}$$

where

$$\begin{aligned}\left.\frac{\partial \mathbf{a}^I_{d_i}}{\partial \mathbf{r}^I_{CM/E}}\right|_{\bar{\mathbf{x}}} = &\left.\frac{\partial \mathbf{g}^I\left(\mathbf{r}^I_{CM/E}\right)}{\partial \mathbf{r}^I_{CM/E}}\right|_{\bar{\mathbf{x}}} \\ &- \left.\frac{\partial \mathbf{g}^I\left(\mathbf{r}^I_{CM/E} + T_{B\to I}\left[\mathbf{r}^B_{a_i/O} - \mathbf{r}^B_{CM/O}\right]\right)}{\partial \mathbf{r}^I_{CM/E}}\right|_{\bar{\mathbf{x}}} \\ &+ \left.\frac{\partial \mathbf{a}^I_{aero}}{\partial \mathbf{r}^I_{CM/E}}\right|_{\bar{\mathbf{x}}} + \left.\frac{\partial \mathbf{a}^I_{SRP}}{\partial \mathbf{r}^I_{CM/E}}\right|_{\bar{\mathbf{x}}}.\end{aligned} \tag{61}$$

Measurement partials with respect to the spacecraft velocity in inertial frame ($\mathbf{v}^I_{CM/E}$) are given as

$$\left.\frac{\partial \boldsymbol{h}}{\partial \mathbf{v}^I_{CM/E}}\right|_{\bar{\mathbf{x}}} = T_{B\to a_i^N} T_{I\to B} \left.\frac{\partial \mathbf{a}^I_{aero}}{\partial \mathbf{v}^I_{CM/E}}\right|_{\bar{\mathbf{x}}}. \tag{62}$$

Measurement partials with respect to the spacecraft's rotation vector ($\theta_{I\to B}$) are given as

$$\left.\frac{\partial \boldsymbol{h}}{\partial \theta_{I\to B}}\right|_{\bar{\mathbf{x}}} = T_{B\to a_i^N} \left.\frac{\partial \mathbf{a}^B_{d_i}}{\partial \theta_{I\to B}}\right|_{\bar{\mathbf{x}}}. \tag{63}$$

Measurement partials with respect to the spacecraft's angular velocity ($\boldsymbol{\omega}^B_{B/I}$) are given as

$$\left.\frac{\partial \boldsymbol{h}}{\partial \boldsymbol{\omega}^B_{B/I}}\right|_{\bar{\mathbf{x}}} = T_{B\to a_i^N} T_{I\to B}\left(\bar{\theta}_{I\to B}\right) \left.\frac{\partial \mathbf{a}^I_{d_i}}{\partial \boldsymbol{\omega}^B_{B/I}}\right|_{\bar{\mathbf{x}}}. \tag{64}$$

Measurement partials with respect to the center of mass position, in spacecraft body-fixed frame and with respect to the origin of the spacecraft body-fixed frame ($\mathbf{r}^B_{CM/O}$), are given as

$$\left.\frac{\partial \boldsymbol{h}}{\partial \mathbf{r}^B_{CM/O}}\right|_{\bar{\mathbf{x}}} = T_{B\to a_i^N} T_{I\to B}\left(\bar{\theta}_{I\to B}\right) \left.\frac{\partial \mathbf{a}^I_{d_i}}{\partial \mathbf{r}^B_{CM/O}}\right|_{\bar{\mathbf{x}}}. \tag{65}$$

Measurement partials with respect to the ballistic coefficient (β), for exponentially decaying atmospheric drag, are given as

$$\left.\frac{\partial \boldsymbol{h}}{\partial \beta}\right|_{\bar{\mathbf{x}}} = T_{B\to a_i^N} T_{I\to B}\left(\bar{\theta}_{I\to B}\right) \left.\frac{\partial \mathbf{a}^I_{d_i}}{\partial \beta}\right|_{\bar{\mathbf{x}}}. \tag{66}$$

Measurement partials with respect to the reference atmospheric density (ρ_r), for exponentially decaying atmospheric drag, are given as

$$\left.\frac{\partial \boldsymbol{h}}{\partial \rho_r}\right|_{\bar{\mathbf{x}}} = T_{B\to a_i^N} T_{I\to B}\left(\bar{\theta}_{I\to B}\right) \left.\frac{\partial \mathbf{a}^I_{d_i}}{\partial \rho_r}\right|_{\bar{\mathbf{x}}}. \tag{67}$$

Measurement partials with respect to the scale height (h_s), for exponentially decaying atmospheric drag, are given as

$$\left.\frac{\partial \boldsymbol{h}}{\partial h_s}\right|_{\bar{\mathbf{x}}} = T_{B\to a_i^N} T_{I\to B}\left(\bar{\theta}_{I\to B}\right) \left.\frac{\partial \mathbf{a}^I_{d_i}}{\partial h_s}\right|_{\bar{\mathbf{x}}}. \tag{68}$$

Measurement partials with respect to the i^{th} accelerometer position, in spacecraft body-fixed frame and with respect to the origin of the spacecraft body-fixed frame ($\mathbf{r}^B_{a_i/O}$), are given as

$$\left.\frac{\partial \boldsymbol{h}}{\partial \mathbf{r}^B_{a_i/O}}\right|_{\bar{\mathbf{x}}} = T_{B\to a_i^N} T_{I\to B}\left(\bar{\theta}_{I\to B}\right) \left.\frac{\partial \mathbf{a}^I_{d_i}}{\partial \mathbf{r}^B_{a_i/O}}\right|_{\bar{\mathbf{x}}}. \tag{69}$$

Detailed derivation of partial derivatives used in Equations (61)-(69) are given in the Appendix.

Measurement partials with respect to the accelerometer bias ($\mathbf{b}_i^{\tilde{a}_i}$) are given as

$$\left.\frac{\partial \boldsymbol{h}}{\partial \mathbf{b}_i^{\tilde{a}_i}}\right|_{\bar{\mathbf{x}}} = I_{3\times 3}. \tag{70}$$

Measurement partials with respect to the accelerometer scale factor ($\mathbf{f}_i^{\tilde{a}_i}$) are given as

$$\left.\frac{\partial \boldsymbol{h}}{\partial \mathbf{f}_i^{\tilde{a}_i}}\right|_{\bar{\mathbf{x}}} = D\left(\bar{\mathbf{a}}_{d_i}^{\tilde{a}_i}\right), \tag{71}$$

where $\bar{\mathbf{a}}_{d_i}^{\tilde{a}_i}$ is given by Equation (52).

Measurement partials with respect to the accelerometer misalignment ($\boldsymbol{\epsilon}_i^{\tilde{a}_i}$) are given as

$$\left.\frac{\partial \boldsymbol{h}}{\partial \boldsymbol{\epsilon}_i^{\tilde{a}_i}}\right|_{\bar{\mathbf{x}}} = \left(I + D\left(\bar{\mathbf{f}}_i^{\tilde{a}_i}\right)\right)\left\{\left[\left(T_{B\to a_i^N} T_{I\to B}\left(\bar{\theta}_{I\to B}\right)\bar{\mathbf{a}}^I_{d_i}\right)\times\right]\right\}, \tag{72}$$

where $\bar{\mathbf{a}}^I_{d_i}$ is given by Equation (53).

Now, the star camera measurement model, as given in Equation (56), is linearized as

$$\delta \tilde{s}^{\tilde{s}} = L_x \delta \mathbf{x} + \boldsymbol{\eta}_{sc}^{\tilde{s}}, \tag{73}$$

where L_x is the measurement partial due to star camera measurements, defined as

$$L_x = \left.\frac{\partial \boldsymbol{l}}{\partial \mathbf{x}}\right|_{\bar{\mathbf{x}}}. \tag{74}$$

Noting that, for this study, only one star camera has been included and because the total number of states is $18 + 12n$ (where n is the number of accelerometers), the measurement partial L_x is a matrix of dimension size $3 \times (18 + 12n)$. Since using Equation (56), it is easy to note that the star camera measurement is only the function of spacecraft rotation vector; this implies

$$\left.\frac{\partial \boldsymbol{l}}{\partial \theta_{I\to B}}\right|_{\bar{\mathbf{x}}} = T_{B\to\tilde{s}} = I_{3\times 3}. \tag{75}$$

As stated earlier, for this study, the misalignments in the setting up of the star camera on the rigid body of the spacecraft have been ignored. Thus, $T_{B\to\tilde{s}}$ is a 3×3 identity matrix.

6 | LINCOV TOOL

6.1 | Summary of linearized dynamics & measurement model

The linearized dynamics in Equation (21) can be summarized as follows:

$$\delta \dot{\mathbf{x}} = F_x \delta \mathbf{x} + G\mathbf{w}, \tag{76}$$

where uppercase characters denote partial derivatives taken with respect to the variable indicated by a subscript and evaluated along the reference state vector (e.g., $F_x = \partial \boldsymbol{f}/\partial \mathbf{x}|_{\bar{\mathbf{x}}}$), and G is a matrix to map the noise vector to the state dynamics.

Now, let the state vector be segmented in two parts such that

$$\mathbf{x} = \begin{bmatrix} \mathbf{x}_1 \\ \mathbf{x}_2 \end{bmatrix} \tag{77}$$

$$\dot{\mathbf{x}} = \begin{bmatrix} \dot{\mathbf{x}}_1 \\ \dot{\mathbf{x}}_2 \end{bmatrix} = \begin{bmatrix} \boldsymbol{f}_1(\mathbf{x}_1, t) \\ \boldsymbol{f}_2(\mathbf{x}_2, t) \end{bmatrix}, \tag{78}$$

where $\mathbf{x}$ is the true state vector, and $\mathbf{x}_1$ and $\mathbf{x}_2$ are defined as

$$\mathbf{x}_1 = \left(\mathbf{r}^I_{CM/E}, \mathbf{v}^I_{CM/E}, \theta_{I\to B}, \boldsymbol{\omega}^B_{B/I}\right)^T \tag{79}$$

$$\mathbf{x}_2 = \left(\mathbf{r}^B_{CM/O}, \beta, \rho_r, h_s, \mathbf{r}^B_{a_i/O}, \mathbf{b}_i^{\tilde{a}_i}, \mathbf{f}_i^{\tilde{a}_i}, \epsilon_i^{\tilde{a}_i}\right)^T, \tag{80}$$

where $\mathbf{x}_2$ denotes all the ECRV.

Thus, based on Equations (76)-(80), F_x can be defined as

$$F_x = \left.\frac{\partial \boldsymbol{f}}{\partial \mathbf{x}}\right|_{\bar{\mathbf{x}}} = \begin{bmatrix} F_{x_1x_1} & F_{x_1x_2} \\ F_{x_2x_1} & F_{x_2x_2} \end{bmatrix}, \tag{81}$$

where F_x is a $(18 + 12n) \times (18 + 12n)$ Jacobian matrix, while $F_{x_1x_1}$ is 12×12, $F_{x_1x_2}$ and $F_{x_2x_1}$ are $12 \times (6 + 12n)$ and $(6 + 12n) \times 12$, and lastly, $F_{x_2x_2}$ is $(6 + 12n) \times (6 + 12n)$, respectively. The number of accelerometers is denoted by n.

$$F_{x_1x_1} = \left.\frac{\partial \boldsymbol{f}_1}{\partial \mathbf{x}_1}\right|_{\bar{\mathbf{x}}} = \begin{bmatrix} Z_{33} & I_{33} & Z_{33} & Z_{33} \\ F_{VR} & F_{VV} & Z_{33} & Z_{33} \\ Z_{33} & Z_{33} & -\Omega_{\otimes} & I_{33} \\ F_{WR} & Z_{33} & F_{W\theta} & F_{WW} \end{bmatrix}_{12\times 12}, \tag{82}$$

where

$$Z_{33} = 0_{3\times 3},\ I_{33} = I_{3\times 3} \tag{83}$$

$$F_{VR} = \left.\frac{\partial \mathbf{g}^I_E\left(\mathbf{r}^I_{CM/E}\right)}{\partial \mathbf{r}^I_{CM/E}}\right|_{\bar{\mathbf{x}}} + \left.\frac{\partial \mathbf{a}^I_{Third-body}}{\partial \mathbf{r}^I_{CM/E}}\right|_{\bar{\mathbf{x}}} + \left.\frac{\partial \mathbf{a}^I_{aero}}{\partial \mathbf{r}^I_{CM/E}}\right|_{\bar{\mathbf{x}}} + \left.\frac{\partial \mathbf{a}^I_{SRP}}{\partial \mathbf{r}^I_{CM/E}}\right|_{\bar{\mathbf{x}}} \tag{84}$$

$$F_{VV} = \left.\frac{\partial \mathbf{a}^I_{aero}}{\partial \mathbf{v}^I_{CM/E}}\right|_{\bar{\mathbf{x}}} \tag{85}$$

$$F_{WR} = J^{-1} \left.\frac{\partial M_{gg}}{\partial \mathbf{r}^I_{CM/E}}\right|_{\bar{\mathbf{x}}} \tag{86}$$

$$F_{W\theta} = J^{-1} \left.\frac{\partial M_{gg}}{\partial \theta}\right|_{\bar{\mathbf{x}}} \tag{87}$$

$$F_{WW} = -J^{-1} \left.\frac{\partial\left(\boldsymbol{\omega}^B_{B/I} \times \left[J\boldsymbol{\omega}^B_{B/I}\right]\right)}{\partial \boldsymbol{\omega}^B_{B/I}}\right|_{\bar{\mathbf{x}}} \tag{88}$$

$$F_{WW} = -J^{-1}\left(-\left[\left(J\bar{\boldsymbol{\omega}}^B_{B/I}\right)\times\right] + \left[\bar{\boldsymbol{\omega}}^B_{B/I}\times\right]J\right). \tag{89}$$

Detailed derivation of partial derivatives used in Equations (84)–(87) are given in the Appendix.

$$F_{x_1x_2} = \left.\frac{\partial \boldsymbol{f}_1}{\partial \mathbf{x}_2}\right|_{\bar{\mathbf{x}}} \tag{90}$$

$$F_{x_1x_2} = \begin{bmatrix} Z_{33} & Z_{31} & Z_{31} & Z_{31} & Z_{33n} & Z_{33n} & Z_{33n} & Z_{33n} \\ Z_{33} & F_{V\beta} & F_{V\rho_r} & F_{Vh_s} & Z_{33n} & Z_{33n} & Z_{33n} & Z_{33n} \\ Z_{33} & Z_{31} & Z_{31} & Z_{31} & Z_{33n} & Z_{33n} & Z_{33n} & Z_{33n} \\ Z_{33} & Z_{31} & Z_{31} & Z_{31} & Z_{33n} & Z_{33n} & Z_{33n} & Z_{33n} \end{bmatrix}. \tag{91}$$

Note that $F_{x_1x_2}$ is a matrix of size $12 \times (6 + 12n)$, respectively. Elements of the matrix in Equation (91) are given below:

$$Z_{31} = 0_{3\times1},\ Z_{33n} = 0_{3\times3n} \tag{92}$$

$$F_{V\beta} = \left.\frac{\partial \mathbf{a}^I_{aero}}{\partial \beta}\right|_{\bar{\mathbf{x}}},\ F_{V\rho_r} = \left.\frac{\partial \mathbf{a}^I_{aero}}{\partial \rho_r}\right|_{\bar{\mathbf{x}}},\ F_{Vh_s} = \left.\frac{\partial \mathbf{a}^I_{aero}}{\partial h_s}\right|_{\bar{\mathbf{x}}}. \tag{93}$$

Detailed derivation of partial derivatives used in Equation (93) are given in the Appendix.

$$F_{x_2x_1} = \left.\frac{\partial \boldsymbol{f}_2}{\partial \mathbf{x}_1}\right|_{\bar{\mathbf{x}}} = 0_{(6+12n)\times12} \tag{94}$$

$$F_{x_2x_2} = \left.\frac{\partial \boldsymbol{f}_2}{\partial \mathbf{x}_2}\right|_{\bar{\mathbf{x}}}. \tag{95}$$

That is,

$$F_{x_2x_2} = \begin{bmatrix} F_{\mathbf{r}_{CM/O}} & Z_{31} & Z_{31} & Z_{31} & Z_{33n} & Z_{33n} & Z_{33n} & Z_{33n} \\ Z_{13} & F_\beta & 0 & 0 & Z_{13n} & Z_{13n} & Z_{13n} & Z_{13n} \\ Z_{13} & 0 & F_{\rho_r} & 0 & Z_{13n} & Z_{13n} & Z_{13n} & Z_{13n} \\ Z_{13} & 0 & 0 & F_{h_s} & Z_{13n} & Z_{13n} & Z_{13n} & Z_{13n} \\ Z_{3n3} & Z_{3n1} & Z_{3n1} & Z_{3n1} & F_{\mathbf{r}_{a_i/O}} & Z_{3n3n} & Z_{3n3n} & Z_{3n3n} \\ Z_{3n3} & Z_{3n1} & Z_{3n1} & Z_{3n1} & Z_{3n3n} & F_{\mathbf{b}_i} & Z_{3n3n} & Z_{3n3n} \\ Z_{3n3} & Z_{3n1} & Z_{3n1} & Z_{3n1} & Z_{3n3n} & Z_{3n3n} & F_{\mathbf{f}_i} & Z_{3n3n} \\ Z_{3n3} & Z_{3n1} & Z_{3n1} & Z_{3n1} & Z_{3n3n} & Z_{3n3n} & Z_{3n3n} & F_{\epsilon_i} \end{bmatrix}. \tag{96}$$

Note that $F_{x_2x_2}$ is a matrix of size $(6 + 12n) \times (6 + 12n)$, respectively. Elements of the matrix in Equation (96) are given below:

$$Z_{13} = 0_{1\times3},\ Z_{13n} = 0_{1\times3n} \tag{97}$$

$$Z_{3n3} = 0_{3n\times3},\ Z_{3n1} = 0_{3n\times1},\ Z_{3n3n} = 0_{3n\times3n} \tag{98}$$

$$F_{\mathbf{r}_{CM/O}} = \left.\frac{\partial \dot{\mathbf{r}}_{CM/O}}{\partial \mathbf{r}_{CM/O}}\right|_{\bar{\mathbf{x}}} = -\frac{I_{3\times3}}{\tau_{\mathbf{r}_{CM/O}}} \tag{99}$$

$$F_\beta = \left.\frac{\partial \dot{\beta}}{\partial \beta}\right|_{\bar{\mathbf{x}}} = -\frac{1}{\tau_\beta} \tag{100}$$

$$F_{\rho_r} = \left.\frac{\partial \dot{\rho}_r}{\partial \rho_r}\right|_{\bar{\mathbf{x}}} = -\frac{1}{\tau_{\rho_r}} \tag{101}$$

$$F_{h_s} = \left.\frac{\partial \dot{h}_s}{\partial h_s}\right|_{\bar{\mathbf{x}}} = -\frac{1}{\tau_{h_s}} \tag{102}$$

$$F_{\mathbf{r}_{a_i/O}} = \left.\frac{\partial \dot{\mathbf{r}}_{a_i/O}}{\partial \mathbf{r}_{a_i/O}}\right|_{\bar{\mathbf{x}}} = -\frac{I_{3n\times3n}}{\tau_{\mathbf{r}_{a_i/O}}} \tag{103}$$

$$F_{\mathbf{b}_i} = \left.\frac{\partial \dot{\mathbf{b}}_i}{\partial \mathbf{b}_i}\right|_{\bar{\mathbf{x}}} = -\frac{I_{3n\times3n}}{\tau_{\mathbf{b}_i}} \tag{104}$$

$$F_{\mathbf{f}_i} = \left.\frac{\partial \dot{\mathbf{f}}_i}{\partial \mathbf{f}_i}\right|_{\bar{\mathbf{x}}} = -\frac{I_{3n\times3n}}{\tau_{\mathbf{f}_i}} \tag{105}$$

$$F_{\epsilon_i} = \left.\frac{\partial \dot{\epsilon}_i}{\partial \epsilon_i}\right|_{\bar{\mathbf{x}}} = -\frac{I_{3n\times3n}}{\tau_{\epsilon_i}}. \tag{106}$$

The linearized accelerometer measurements can be summarized as follows:

$$\delta\tilde{a}_i^{\tilde{a}_i} = \left[\left.\frac{\partial \boldsymbol{h}_{3n}}{\partial \mathbf{r}^I_{CM/E}}\right|_{\bar{\mathbf{x}}} \left.\frac{\partial \boldsymbol{h}_{3n}}{\partial \mathbf{v}^I_{CM/E}}\right|_{\bar{\mathbf{x}}} \left.\frac{\partial \boldsymbol{h}_{3n}}{\partial \theta_{I\to B}}\right|_{\bar{\mathbf{x}}} \left.\frac{\partial \boldsymbol{h}_{3n}}{\partial \boldsymbol{\omega}^B_{B/I}}\right|_{\bar{\mathbf{x}}} \left.\frac{\partial \boldsymbol{h}_{3n}}{\partial \mathbf{r}^B_{CM/O}}\right|_{\bar{\mathbf{x}}} \left.\frac{\partial \boldsymbol{h}_{3n}}{\partial \beta}\right|_{\bar{\mathbf{x}}} \left.\frac{\partial \boldsymbol{h}_{3n}}{\partial \rho_r}\right|_{\bar{\mathbf{x}}} \left.\frac{\partial \boldsymbol{h}_{3n}}{\partial h_s}\right|_{\bar{\mathbf{x}}} \left.\frac{\partial \boldsymbol{h}_{3n}}{\partial \mathbf{r}^B_{a_i/O}}\right|_{\bar{\mathbf{x}}} \left.\frac{\partial \boldsymbol{h}_{3n}}{\partial \mathbf{b}_i^{\tilde{a}_i}}\right|_{\bar{\mathbf{x}}} \left.\frac{\partial \boldsymbol{h}_{3n}}{\partial \mathbf{f}_i^{\tilde{a}_i}}\right|_{\bar{\mathbf{x}}} \left.\frac{\partial \boldsymbol{h}_{3n}}{\partial \epsilon_i^{\tilde{a}_i}}\right|_{\bar{\mathbf{x}}}\right]_{3n\times(18+12n)} \delta\mathbf{x} + \boldsymbol{\eta}_i^{\tilde{a}_i}, \tag{107}$$

where partials in Equation (107) are given in Section 5.2.

Similarly, the linearized star camera measurements can be summarized as follows:

$$\delta\tilde{s}^{\tilde{s}} = [0_{3\times3} \quad 0_{3\times3} \quad I_{3\times3} \quad 0_{3\times3} \quad 0_{3\times3} \quad 0_{3\times1} \quad 0_{3\times1} \quad 0_{3\times1} \quad 0_{3\times3n} \quad 0_{3\times3n} \quad 0_{3\times3n}]_{3\times(18+12n)}\delta\mathbf{x} + \boldsymbol{\eta}_{sc}^{\tilde{s}}, \tag{108}$$

where partials in Equation (108) are given in Section 5.2.

6.2 | LinCov models - theory & setup

Techniques like the Monte Carlo analysis and Linear Covariance analysis are extensively used for modeling and simulating a range of possible operational scenarios and thereby enable the study of the effects of significant

parameters on the overall mission performance. These techniques are particularly useful for guidance, navigation, and control (GN&C) analysis and generally include the effects of environment, actuator, and sensor uncertainties; estimation errors; and most importantly, the effect of uncertainties and estimation errors on trajectory and attitude control errors (Geller, 2006).

Despite the initial overhead associated with the development of linear models, LinCov techniques have cost benefits when compared to Monte Carlo analysis (Geller, 2006). This is because LinCov techniques produce the representative results in a fraction of the time, thus saving a tremendous amount of computational power and time (Geller, 2006). Since the expected envelope of trajectories about the nominal is often very small for a general orbital dynamics problem, the conditions under which LinCov is valid (e.g., good linear models) are easily satisfied (Geller, 2006).

In a Linear Covariance approach, the system states are segmented into two parts, viz. filter states and truth states. Where the truth states are the same as the filter states, except the difference between the truth gravitational model and filter gravitational model. The filter gravitational model is of low resolution in comparison to the truth gravitational model. Both state vectors include stochastic realizations and are initialized with the nominal values of the states.

Further, the covariance of the filter states and the augmented states (truth and filter) are defined such that the filter state covariance ($\hat{P}$) is the same as the truth state covariance (in the augmented state covariance P_A). However, the filter covariance (in the augmented state covariance P_A) is a zero matrix. These covariances (and P_A) are propagated and updated so as to generate the covariance of the dispersions and navigation errors in a single simulation run.

The filter state covariance $\hat{P}$ and the augmented state covariance P_A are propagated as follows (Christensen & Geller, 2014):

$$\hat{P}(t_{k+1}) = \hat{\phi}\hat{P}(t_k)\hat{\phi}^T + \hat{Q}_d \tag{109}$$

$$P_A(t_{k+1}) = \phi P_A(t_k)\phi^T + Q_d, \tag{110}$$

where $\hat{\phi}$ and ϕ are the filter and augmented state transition matrices, defined as

$$\hat{\phi} = e^{\hat{F}_x dt} \tag{111}$$

$$\phi = e^{\left(\begin{bmatrix} F_x & 0_{z\times\hat{z}} \\ 0_{\hat{z}\times z} & \hat{F}_x \end{bmatrix} dt\right)} \tag{112}$$

$$\hat{F}_x = \left.\frac{\partial \boldsymbol{f}}{\partial \hat{\mathbf{x}}}\right|_{\bar{\mathbf{x}}}, \tag{113}$$

where F_x and $\hat{F}_x$ are the true and filter state Jacobian given by Equation (81) and Equation (113), and z and $\hat{z}$ represent the number of truth and filter states, respectively.

Now, since for this study the filter state model has the same states as the truth state model and because the only notable difference between two models is the resolution of the gravity model, the partial derivatives needed to compute $\hat{F}_x$ are the same (except the gravity partials) as that needed for F_x, given in Section 6.1.

For this study, the resolution of the truth gravity model has been set to 18×18, whereas the resolution of the filter gravity model is set to 12×12. Details about filter and truth models are also noted, alongside the results, in Section 8.

In Equation (109) and Equation (110), $\hat{Q}_d$ and Q_d are the filter and augmented process noise covariance matrices for the filter and augmented states.

For the accelerometer measurements, the filter $\hat{P}$ covariance is updated as follows (Christensen & Geller, 2014):

$$\begin{aligned}\hat{P}\left(t_k^+\right) = &\left[I - \hat{K}(t_k)\hat{H}_{\hat{x}}(t_k)\right]\hat{P}(t_k)\left[I - \hat{K}(t_k)\hat{H}_{\hat{x}}(t_k)\right]^T \\ &+ \hat{K}(t_k)\hat{R}_a(t_k)\hat{K}^T(t_k)\end{aligned} \tag{114}$$

$$\hat{K}(t_k) = \hat{P}(t_k)\hat{H}_{\hat{x}}^T(t_k)\left[\hat{H}_{\hat{x}}(t_k)\hat{P}(t_k)\hat{H}_{\hat{x}}^T(t_k) + \hat{R}_a(t_k)\right]^{-1} \tag{115}$$

$$\hat{H}_{\hat{x}} = \left.\frac{\partial \boldsymbol{h}}{\partial \hat{\mathbf{x}}}\right|_{\bar{\mathbf{x}}}, \tag{116}$$

where $\hat{K}(t_k)$ is the Kalman gain, and $\hat{H}_{\hat{x}}(t_k)$ is the filter measurement partial matrix given by Equation (116) (for accelerometer measurements).

In Equation (114) and Equation (115), the filter measurement noise covariance is denoted by $\hat{R}_a(t_k)$ and is given by

$$E[\hat{\boldsymbol{\eta}}_i^{\tilde{a}_i}(t)\hat{\boldsymbol{\eta}}_i^{\tilde{a}_i}(t')^T] = Q_{\hat{\eta}_i}\delta(t - t') \tag{117}$$

$$\hat{R}_a(t_k) = \frac{Q_{\hat{\eta}_i}}{\delta t_{meas}}, \tag{118}$$

where $\hat{\boldsymbol{\eta}}_i^{\tilde{a}_i}$ is the accelerometer measurement noise, modeled as zero-mean white Gaussian noise, used in the filter model. The strength of the accelerometer measurement noise is denoted by $Q_{\hat{\eta}_i}$, and δt_{meas} is the measurement update time in seconds, as used in the filter model. Note the size of $\hat{R}_a(t_k)$ is $3n \times 3n$, where n is the number of accelerometers onboard.

The augmented P_A covariance is updated as follows (Christensen & Geller, 2014):

$$P_A(t_k^+) = A_k(t_k)P_A(t_k)A_k^T(t_k) + B_k(t_k)R_a(t_k)B_k^T(t_k) \tag{119}$$

$$A_k(t_k) = \begin{bmatrix} I_{z\times z} & 0_{z\times\hat{z}} \\ \hat{K}(t_k)H_x(t_k) & I_{\hat{z}\times\hat{z}} - \hat{K}(t_k)\hat{H}_{\hat{x}}(t_k) \end{bmatrix} \quad (120)$$

$$B_k(t_k) = \begin{bmatrix} 0_{z\times(z+\hat{z})} \\ \hat{K}(t_k) \end{bmatrix}, \quad (121)$$

where $H_x(t_k)$ is the truth measurement partial matrix given by Equation (58) (for accelerometer measurements), and $R_a(t_k)$ is the truth measurement noise covariance given by Equation (47) (for accelerometer measurements), respectively. In Equation (120) and Equation (121), z and $\hat{z}$ represent the number of truth and filter states.

As stated earlier, the filter state model has the same states as the truth state model, and because the only notable difference between two models is the resolution of the gravity model, the partial derivatives needed to compute $\hat{H}_{\hat{x}}(t_k)$ are the same (except the gravity partials) as that needed for $H_x(t_k)$, given in Section 5.2.

For the star camera measurements, the filter $\hat{P}$ covariance is updated as follows (Christensen & Geller, 2014):

$$\hat{P}(t_k^+) = \left[I - \hat{K}(t_k)\hat{L}_{\hat{x}}(t_k)\right]\hat{P}(t_k)\left[I - \hat{K}(t_k)\hat{L}_{\hat{x}}(t_k)\right]^T + \hat{K}(t_k)\hat{R}_{sc}(t_k)\hat{K}^T(t_k) \quad (122)$$

$$\hat{K}(t_k) = \hat{P}(t_k)\hat{L}_{\hat{x}}^T(t_k)\left[\hat{L}_{\hat{x}}(t_k)\hat{P}(t_k)\hat{L}_{\hat{x}}^T(t_k) + \hat{R}_{sc}(t_k)\right]^{-1} \quad (123)$$

$$\hat{L}_{\hat{x}} = \left.\frac{\partial \boldsymbol{l}}{\partial \hat{\mathbf{x}}}\right|_{\bar{\mathbf{x}}}, \quad (124)$$

where $\hat{K}(t_k)$ is the Kalman gain, and $\hat{L}_{\hat{x}}(t_k)$ is the filter measurement partial matrix given by Equation (124) (for star camera measurements).

In Equation (122) and Equation (123), the filter measurement noise covariance is denoted by $\hat{R}_{sc}(t_k)$ and is given by

$$E[\hat{\boldsymbol{\eta}}_{sc,i}^{\tilde{s}}\hat{\boldsymbol{\eta}}_{sc,j}^{\tilde{s}\,T}] = Q_{\hat{\eta}_{sc}}\delta_{ij}, \quad (125)$$

where δ_{ij} is a Kronecker delta function, and $\hat{\boldsymbol{\eta}}_{sc}^{\tilde{s}}$ is a vector of zero-mean white Gaussian noise on the star camera measurements, as used in the filter model. The covariance of the measurement noise for the star camera measurements is denoted by $Q_{\hat{\eta}_{sc}}(rad^2)$, i.e.,

$$\hat{R}_{sc}(t_k) = Q_{\hat{\eta}_{sc}}. \quad (126)$$

Note the size of $\hat{R}_{sc}(t_k)$ is $3n \times 3n$, where n is the number of star cameras onboard.

The augmented P_A covariance is updated as follows (Christensen & Geller, 2014):

$$P_A(t_k^+) = A_k(t_k)P_A(t_k)A_k^T(t_k) + B_k(t_k)R_{sc}(t_k)B_k^T(t_k) \quad (127)$$

$$A_k(t_k) = \begin{bmatrix} I_{z\times z} & 0_{z\times\hat{z}} \\ \hat{K}(t_k)L_x(t_k) & I_{\hat{z}\times\hat{z}} - \hat{K}(t_k)\hat{L}_{\hat{x}}(t_k) \end{bmatrix} \quad (128)$$

$$B_k(t_k) = \begin{bmatrix} 0_{z\times(z+\hat{z})} \\ \hat{K}(t_k) \end{bmatrix}, \quad (129)$$

where $L_x(t_k)$ is the truth measurement partial matrix given by Equation (74) (for star camera measurements), and $R_{sc}(t_k)$ is the truth measurement noise covariance given by Equation (55) (for star camera measurements), respectively. In Equation (128) and Equation (129), z and $\hat{z}$ represent the number of truth and filter states.

As stated earlier, the filter state model has the same states as the truth state model, and because the only notable difference between two models is the resolution of the gravity model, the partial derivatives needed to compute $\hat{L}_{\hat{x}}(t_k)$ are the same (except the gravity partials) as that needed for $L_x(t_k)$, given in Section 5.2.

7 | PROCEDURE

7.1 | Performance metric & evaluation

Performance metrics for this research are the navigation solution at the final time, i.e., the standard deviation (three-sigma values) for the spacecraft position, velocity, attitude, angular velocity, center of mass position, accelerometer positions, and accelerometer parameters (bias, scale factor, and misalignment). Final navigation requirements are defined based on the mission type, and these requirements are compared to the performance metrics of the autonomous navigation system based on advanced accelerometers.

Final navigation requirements are defined in the Local Vertical and Local Horizontal (LVLH) frame, and the final navigation solution in the LVLH frame is compared with the pre-defined requirements. Error budgets are used to show the contribution of each source of error to the final orbit navigation error, which in turn is compared against the reference solution for different mission types.

Covariance of the true navigation state errors P_{true} and covariance of the filter state errors $\hat{P}$ are used to evaluate

the performance of the onboard navigation system.

$$P_{true} = \left[-M_x \; I_{\hat{z}\times\hat{z}}\right] P_A \left[-M_x \; I_{\hat{z}\times\hat{z}}\right]^T, \tag{130}$$

where M_x is the partial with respect to the true state of the mapping function defined as (Christensen, 2013)

$$M_x = I_{\hat{z}\times z}. \tag{131}$$

True navigation error provides insight into the navigation performance. The true navigation error is also used for sensitivity analysis, where the simulation is run multiple times with the combination of different error groups switched on/off in the truth model (while the filter model remains unchanged), to compute the error budget or relative contribution of each error group, respectively.

7.2 | Error budget analysis

Error budget analysis, also known as sensitivity analysis, is a tool to compute the contribution of different sources of error to the total error. This is significant as based on this analysis, individual components of a navigation systems, or GN&C in general, can be adjusted and designed while having permissible and predictable performance as per mission requirements.

In an error budget analysis, the total error is always equal to the root sum square (RSS) of the individual error sources, provided the error sources are uncorrelated. The selection and classification of the error sources depend entirely on the mission requirements and known/unknown parameters.

For this study, the sources of error have been classified into nine groups:

1. Spacecraft's initial position and velocity uncertainty - In the plots, this group is denoted by an acronym PosVel.
2. Spacecraft's initial orientation and angular velocity uncertainty - In the plots, this group is denoted by an acronym AttdAV.
3. Spacecraft's center of mass position uncertainty - In the plots, this group is denoted by an acronym COMPos.
4. Translational process noise - In the plots, this group is denoted by an acronym QTErr.
5. Rotational process noise - In the plots, this group is denoted by an acronym QRErr.
6. Uncertainty in atmospheric model parameters (spacecraft ballistic coefficient, reference atmospheric density, and scale height) - In the plots, this group is denoted by an acronym AtmErr.
7. Uncertainty in accelerometer parameters (accelerometer measurement noise, bias, scale factor, and misalignment) - In the plots, this group is denoted by an acronym ACErr.
8. Accelerometer position uncertainty - In the plots, this group is denoted by an acronym ACPos.
9. Star camera measurement noise - In the plots, this group is denoted by an acronym SCNoise.

Uncertainty/Error due to each of the individual groups is switched on for the truth model, while all other sources of error (in the truth model) are switched off. The filter model remains unchanged, and the contribution due to this error group on the true navigation error of each state is determined in a single simulation run. Thus, with a single simulation run, the range of acceptable uncertainty in the particular error group for a given mission requirement can be determined. Based on nine simulation runs, an error budget analysis is conducted, and the results are used to design an autonomous orbital navigation system.

Note that this classification of error groups is for this study and is not unique; it depends on the knowledge of the system and mission requirements. However, the error sources must be uncorrelated.

Generally, an additional simulation run with all the errors switched on for both the truth and filter model to validate the error budget analysis.

8 | SIMULATION RESULTS & ANALYSIS

8.1 | Initial setup

Initial setup of the simulation parameters and the nominal values for initial state errors/uncertainties are presented in this section. Spacecraft specifications, nominal values of atmospheric drag model parameters, initial conditions, time constants, accelerometer parameters, star camera parameters, and environmental uncertainties are given in Tables 2–7.

Initial conditions, as defined in Table 3, are the initial uncertainties on the state vector. These uncertainties are used to initialize the filter state covariance ($\hat{P}$) and the truth state covariance (in the augmented state covariance P_A), respectively.

Further, the time constants, as defined in Table 4, are used to model the ECRVs in the state vector.

For the results presented in the forthcoming sections, three accelerometers with a baseline of 0.5 m and a measurement update frequency of 20 sec are used. A plot of the accelerometer configuration is shown in Figure 5.

Specifications for parameters given above have been set as per the recent advancements made in the development

TABLE 2 Spacecraft (s/c) specifications and nominal value of atmospheric drag parameters

Parameter name		Nominal value	Units
Spacecraft (s/c) parameters	Radius	0.3	meters (m)
	Mass	406.965	kg
	Coefficient of diffuse reflection	2	unit-less
	Inertia	11.40 (along X-X)	$kg.m^2$
		10.93 (along Y-Y)	$kg.m^2$
		10.93 (along Z-Z)	$kg.m^2$
	Coefficient of drag	2	unit-less
Atmospheric drag parameters	Ballistic number	5.56×10^{-3}	m^2/kg
	Reference atmospheric density	2.80×10^{-12}	kg/m^3
	Reference scale height	58019	meters (m)

TABLE 3 Initial conditions - spacecraft (s/c) position, velocity, attitude, and angular velocity

Initial conditions	1σ value	Units	
Spacecraft (s/c) position	radial	500	meters (m)
	cross-track	1000	meters (m)
	along-track	1000	meters (m)
Spacecraft (s/c) velocity	radial	1.0	m/s
	cross-track	1.0	m/s
	along-track	1.0	m/s
Spacecraft (s/c) attitude	radial	10^{-3}	radians (rad)
	cross-track	10^{-3}	radians (rad)
	along-track	10^{-3}	radians (rad)
velocity	cross-track	10^{-5}	rad/s
	along-track	10^{-5}	rad/s

TABLE 4 Time Constants (T denotes the orbital period)

Parameter name	Value	Units
Ballistic number	1000T	seconds (s)
Reference atmospheric density	1000T	seconds (s)
Reference scale height	1000T	seconds (s)
Center of mass (COM) position	T/2	seconds (s)
Accelerometer (AC) position, bias, scale-factor, misalignment	T/2	seconds (s)

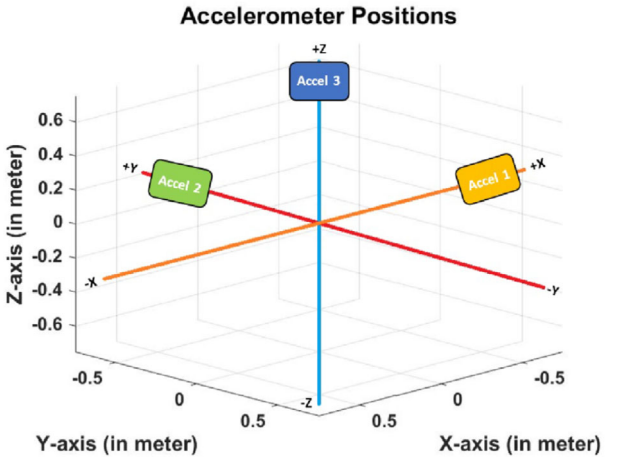

FIGURE 5 Accelerometer configuration [Color figure can be viewed in the online issue, which is available at wileyonlinelibrary.com and www.ion.org]

of precision sensors and future projections mentioned in the relevant literature (Kasevich, 2006, 2007; Silvestrin et al., 2012; Zhu et al., 2013).

8.2 | LinCov results

The reference orbit is defined by the orbital parameters tabulated below.

The key performance characteristic, considered here, is the final time true navigation error. The true navigation error is defined as the difference between the navigation state vector and the corresponding true state vector; the covariance matrix of the true navigation error is extracted from the augmented covariance matrix. This performance characteristic is important as it helps to quantify the filter performance based on the comparison of the solution from the filter and the truth, respectively.

Also, in the results, the major contributing error groups have been labelled as error source 1, 2, and 3, where the error contribution (towards the RSS of all the error sources) due to error source 1 is more than that due to the error source 2, which in turn is more than that due to the error source 3, respectively.

Results for LEO (50-deg inclination) are presented. To model high sensor grade and precise system model, sensor parameters, environmental uncertainties, and initial 1σ errors for all states are set equal to the values given in

TABLE 5 Accelerometer (AC) parameters

Parameter name	High cost	Moderate cost	Low cost	Units
Number of accelerometers (AC)	3, 6	3, 6	3, 6	unit-less
Accelerometer baseline	0.5, 1.0	0.5, 1.0	0.5, 1.0	meters (m)
Accelerometer measurement update frequency	20	20	20	seconds (s)
Accelerometer measurement noise resolution	10^{-13}	10^{-11}	10^{-10}	$m/s^2\sqrt{Hz}$
1σ Accelerometer position	10^{-5}	10^{-4}	10^{-3}	meters (m)
1σ Accelerometer bias	10^{-5}	10^{-4}	10^{-3}	unit-less
1σ Accelerometer scale-factor	10^{-11}	10^{-9}	10^{-7}	m/s^2
1σ Accelerometer misalignment	10^{-6}	10^{-5}	10^{-4}	radians (rad)

TABLE 6 Star Camera (SC) parameters

Parameter name	High cost	Moderate cost	Low cost	Units
Number of star cameras (SC)	1	1	1	unit-less
Star camera measurement update frequency	20	20	20	seconds (s)
Star camera measurement noise resolution	10^{-4}	10^{-4}	10^{-3}	radians (rad)

the High Cost column of Tables 5, 6, and 7. Results have been generated by setting the parameters as per the values given in Tables 2, 3, and 8.

First, the results are presented for three accelerometers with initial 1σ error on spacecraft position, velocity, attitude, and angular velocity set equal to the values given in Table 3, accelerometer parameters are set as per Table 5, and the time constants are set as per Value 1 in Table 4.

Results for the true navigation error 1σ standard deviation on spacecraft position and attitude are shown in Figures 6–7. These results are for the inertially fixed case, i.e., non-rotating spacecraft.

The true navigation error 1σ standard deviation for all states converge to a steady-state value. However, the estimates for accelerometer states are poor, especially accelerometer misalignment. This means that with the given system (dynamics and measurements), the uncertainty on the accelerometer states did not converge to a steady-state value. One of the reasons for poor estimation of accelerometer states could be weak observability of these states. The error budget results for accelerometer states also reflect this, because the major source of error is accelerometer error.

Further, plots for spacecraft velocity and angular velocity are not shown, as the trend for these states is similar to the trend of the true navigation error for spacecraft position and orientation. All the plots have been annotated to depict the major sources of true navigation error.

Error budget results are summarized in Table 9. Note that the total steady-state true navigation error is the RSS of all the error sources.

TABLE 7 Environmental Uncertainties

Parameter name	High cost	Moderate cost	Low cost	Units
Truth gravity model	18×18	18×18	18×18	unit-less
Filter gravity model	12×12	12×12	12×12	unit-less
1σ reference atm. density	2.80×10^{-15}	2.80×10^{-14}	2.80×10^{-13}	kg/m^3
1σ reference scale height	58.019	580.19	5801.9	meters (m)
Translational process noise	10^{-10} $(\sim 52\ m/rev\ 3\sigma)$	10^{-08} $(\sim 520\ m/rev\ 3\sigma)$	10^{-08} $(\sim 520\ m/rev\ 3\sigma)$	m^2/s^3
Aerodynamic process noise	10^{-10} $(\sim 52\ m/rev\ 3\sigma)$	10^{-08} $(\sim 520\ m/rev\ 3\sigma)$	10^{-08} $(\sim 520\ m/rev\ 3\sigma)$	m^2/s^3
Rotational process noise	10^{-16} $(\sim 0.03\ rad/rev\ 3\sigma)$	10^{-14} $(\sim 0.3\ rad/rev\ 3\sigma)$	10^{-14} $(\sim 0.3\ rad/rev\ 3\sigma)$	$1/s^3$
1σ spacecraft (s/c) ballistic number	5.56×10^{-6}	5.56×10^{-5}	5.56×10^{-4}	m^2/kg
1σ spacecraft (s/c) (COM) position	10^{-4}	10^{-3}	10^{-2}	meters (m)

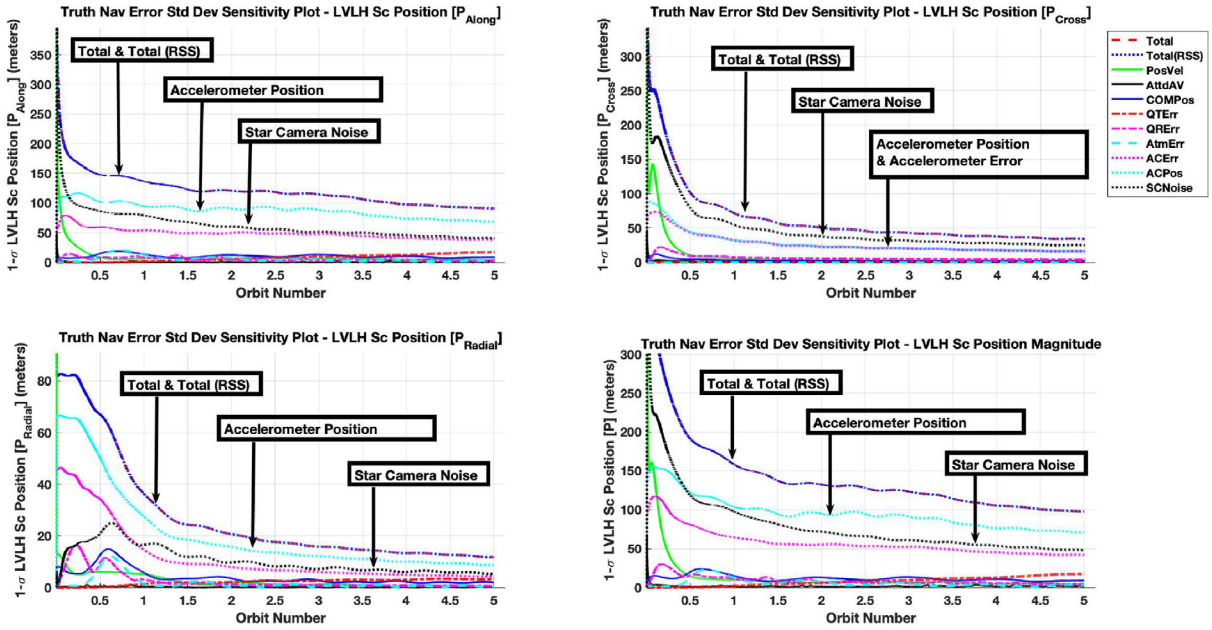

FIGURE 6 True navigation error 1σ std. deviation on spacecraft position components (in LVLH frame) & magnitude. For a non-rotating s/c in LEO 50 deg. inc. orbit, with 3 accel., 0.5 m baseline length, large time constant, & high cost model. [Color figure can be viewed in the online issue, which is available at wileyonlinelibrary.com and www.ion.org]

Results for the true navigation error 1σ standard deviation on spacecraft position and attitude are shown in Figures 8–9, for the rotating Nadir pointing spacecraft.

The true navigation error 1σ standard deviation for all states converge to a steady-state value. However, the estimates for accelerometer states do not converge to a steady-state value, especially accelerometer misalignment. The reason for poor estimation of accelerometer states is suspected to be weak observability of these states. The error budget results for accelerometer states also reflect this, because the major source of error is accelerometer error.

Further, plots for spacecraft velocity and angular velocity are not shown as the trend for these states is similar to the trend of the true navigation error for spacecraft position and orientation. All the results have been annotated to depict the major sources of true navigation error.

Error budget results are summarized in Table 10. Note that the total steady-state true navigation error is the RSS of all the error sources.

The results in Table 10 show that the estimates for the spacecraft position, velocity, attitude, angular velocity, and atmospheric parameter states improve (by about 2% in position and 34% in attitude) for the rotating spacecraft in comparison to that for the non-rotating spacecraft, whereas the estimates for the spacecraft's center of mass position are marginally better for the non-rotating spacecraft. Estimates for accelerometer states show no change for the rotating spacecraft.

Correspondingly, the results for the moderate sensor grade and moderately precise system model were generated using the values given in the Moderate Cost column of Tables 5, 6, and 7. It was found that the filter performance degrades and depicts the effect of the lower sensor grade

TABLE 8 Orbital Parameters of LEO (50-degree Inclination) and Polar LEO

Name	Value (LEO 50° inc.)	Value (Polar LEO)	Units
Semi-major axis (a)	7×10^6	7080136.3	meters (m)
Eccentricity (e)	10^{-2}	1.37×10^{-4}	unit-less
Inclination (i)	50	98.2194	degree (deg)
Argument of perifocus (ω)	30	89.4379	degree (deg)
Right ascension of the ascending node (Ω)	60	298.3267	degree (deg)
True anomaly (ν)	120	0	degree (deg)
Numerical integration time-step	10	10	seconds (s)
Number of orbits simulated	5	5	unit-less

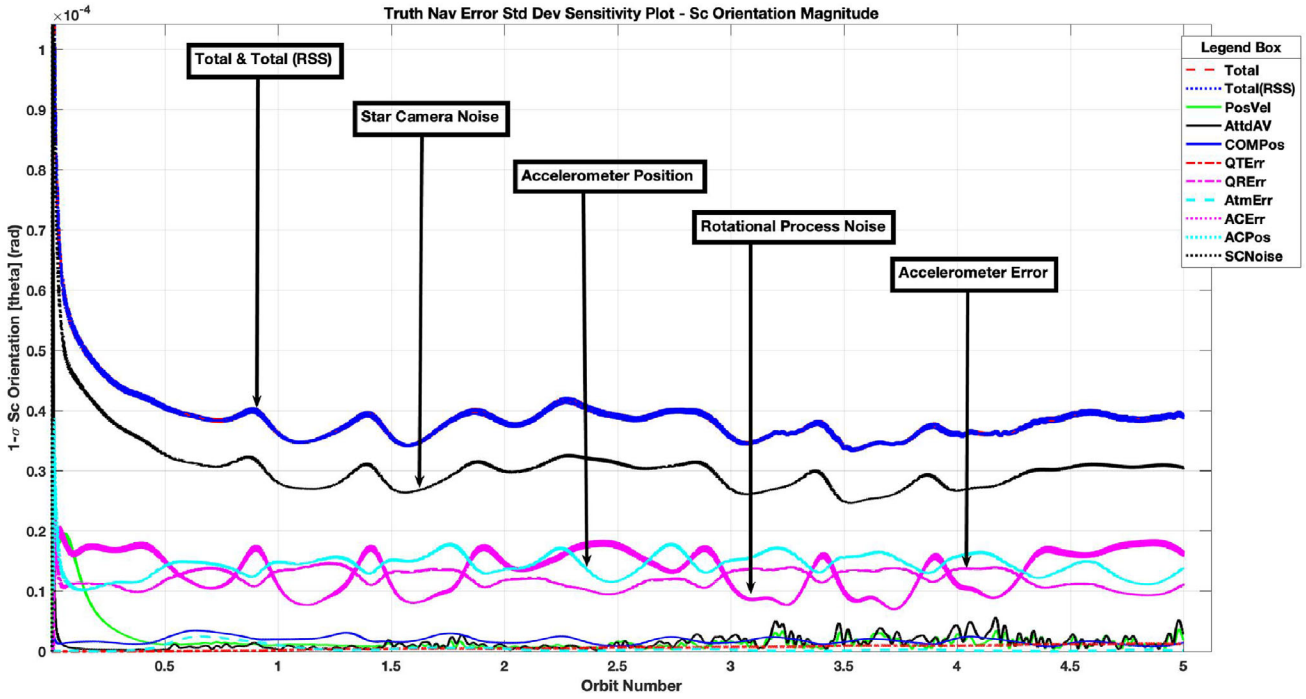

FIGURE 7 True navigation error 1σ std. deviation on spacecraft attitude magnitude. For a non-rotating s/c in LEO 50 deg. inc. orbit, with 3 accel., 0.5 m baseline length, large time constant, & high cost model. [Color figure can be viewed in the online issue, which is available at wileyonlinelibrary.com and www.ion.org]

TABLE 9 Error budget of the maximum steady-state true navigation error 1σ std. deviation. For a non-rotating s/c in LEO 50 deg. inc. orbit, with 3 accel., 0.5 m baseline length, large time constant, & high cost model

State name	Total steady-state true navigation error 1σ	Error source 1	Error source 2	Error source 3	Units
Spacecraft Position Magnitude	105.36	Accelerometer Position - 76.20	Star Camera Noise - 53.89	Accelerometer Error - 45.34	m
Spacecraft Velocity Magnitude	0.11	Accelerometer Position - 0.08	Star Camera Noise - 0.06	Accelerometer Error - 0.05	m/s
Spacecraft Attitude Magnitude	4.032×10^{-5}	Star Camera Noise - 3.137×10^{-5}	Rotational Process Noise - 1.6535×10^{-5}	Accelerometer Position - 1.5211×10^{-5}	rad
Spacecraft Angular Velocity Magnitude	2.0629×10^{-7}	Rotational Process Noise - 1.6269×10^{-7}	Accelerometer Position - 7.4626×10^{-8}	Star Camera Noise - 7.4081×10^{-8}	rad/s

on the true navigation error of spacecraft position, velocity, attitude, and angular velocity. The accelerometer error is a major source of error and thus the system should be designed accordingly.

Expectedly, filter performance worsens when the low sensor grade and less precise system model is simulated using the values given in the Low Cost column of Tables 5, 6, and 7. The true navigation error for spacecraft position and velocity diverge, and the estimation of these states is not feasible. The major source of error is due to the low grade sensor model and its associated accelerometer error. Though estimation of spacecraft attitude and angular velocity is still possible because of the star camera measurements.

Further, results for Polar LEO are presented. Filter performance is found to be about 20-35% better than that for the LEO 50-degree inclination orbit for the corresponding scenarios. To model the high sensor grade and precise system model, sensor parameters, environmental uncertainties, and initial 1σ error for all states are set equal

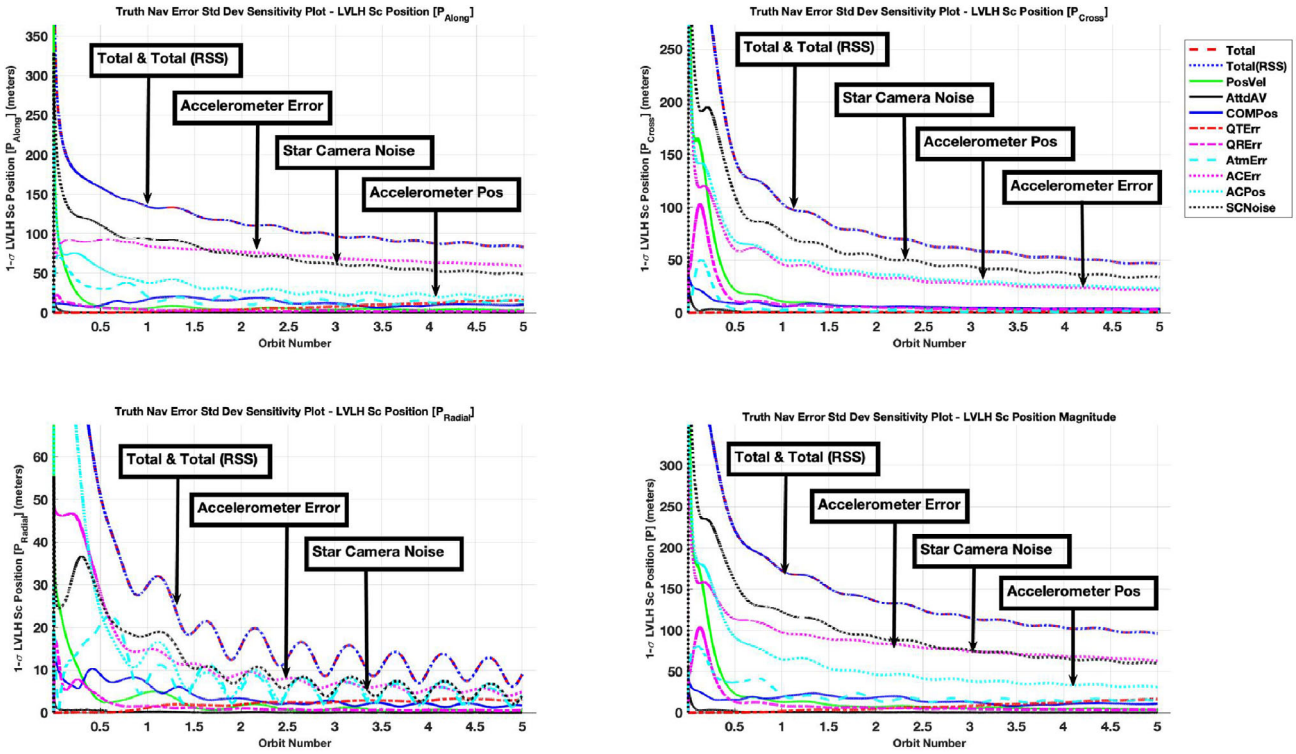

FIGURE 8 True navigation error 1σ std. deviation on spacecraft position components (in LVLH frame) & magnitude. For a rotating s/c in LEO 50 deg. inc. orbit, with 3 accel., 0.5 m baseline length, large time constant, & high cost model [Color figure can be viewed in the online issue, which is available at wileyonlinelibrary.com and www.ion.org]

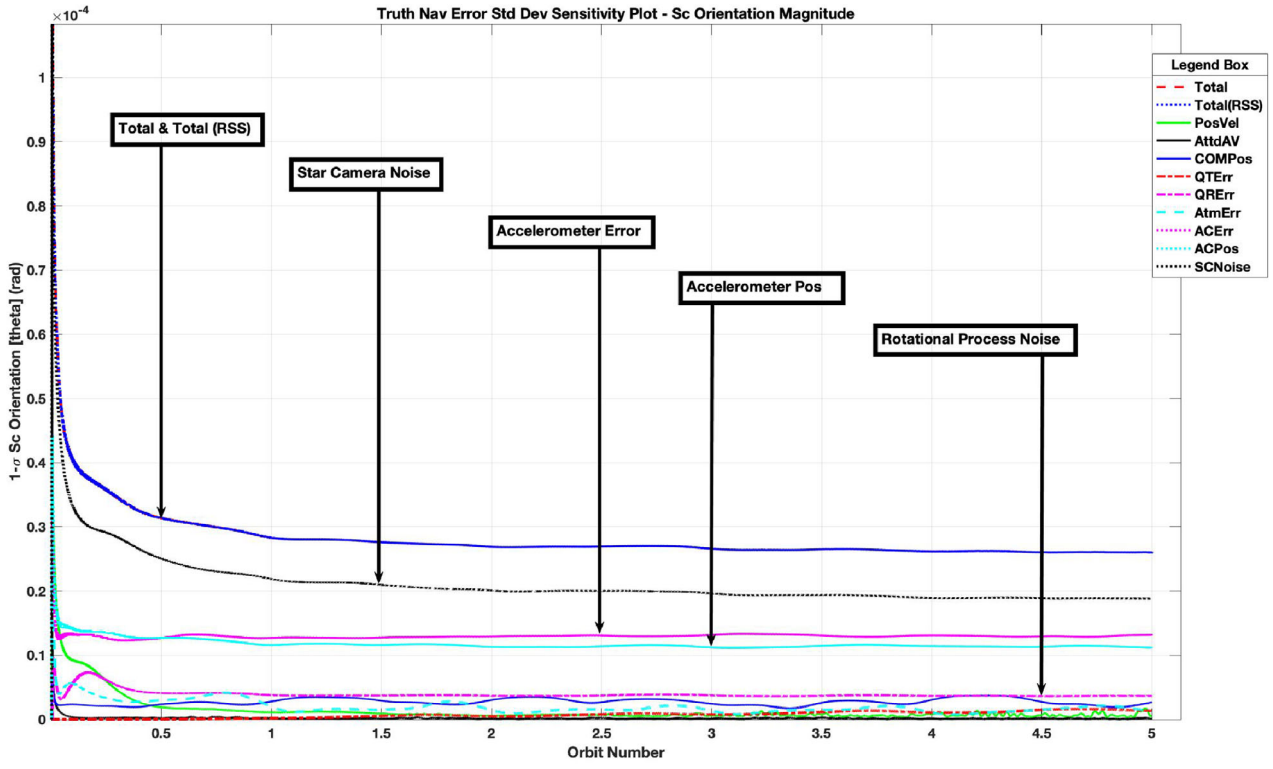

FIGURE 9 True navigation error 1σ std. deviation on spacecraft attitude magnitude. For a rotating s/c in LEO 50 deg. inc. orbit, with 3 accel., 0.5 m baseline length, large time constant, & high cost model [Color figure can be viewed in the online issue, which is available at wileyonlinelibrary.com and www.ion.org]

TABLE 10 Error budget of the maximum steady-state true navigation error 1σ std. deviation. For a rotating s/c in LEO 50 deg. inc. orbit, with 3 accel., 0.5 m baseline length, large time constant, & high cost model

State name	Total steady-state True navigation error 1σ	Error source 1	Error source 2	Error source 3	Units
Spacecraft Position Magnitude	103.33	Accelerometer Error - 68.32	Star Camera Noise - 66.11	Accelerometer Position - 34.10	m
Spacecraft Velocity Magnitude	0.11	Accelerometer Error - 0.07	Star Camera Noise - 0.07	Accelerometer Position - 0.04	m/s
Spacecraft Attitude Magnitude	2.6354×10^{-5}	Star Camera Noise - 1.8959×10^{-5}	Accelerometer Error - 1.312×10^{-5}	Accelerometer Position - 1.1457×10^{-5}	rad
Spacecraft Angular Velocity Magnitude	7.8497×10^{-8}	Rotational Process Noise - 5.6284×10^{-8}	Accelerometer Error - 3.4877×10^{-8}	Accelerometer Position - 3.1892×10^{-8}	rad/s

TABLE 11 Error budget of the maximum steady-state true navigation error 1σ std. deviation. For a non-rotating s/c in Polar LEO orbit, with 3 accel., 0.5 m baseline length, large time constant, & high cost model

State name	Total steady-state True navigation Error 1σ	Error source 1	Error source 2	Error source 3	Units
Spacecraft Position Magnitude	84.07	Accelerometer Position - 71.16	Accelerometer Error - 41.94	Translational Process Noise - 10.79	m
Spacecraft Velocity Magnitude	0.09	Accelerometer Position - 0.07	Accelerometer Error - 0.04	Translational Process Noise - 0.01	m/s
Spacecraft Attitude Magnitude	1.0178×10^{-5}	Star Camera Noise - 7.7697×10^{-6}	Rotational Process Noise - 4.4302×10^{-6}	Accelerometer Position - 2.9721×10^{-6}	rad
Spacecraft Angular Velocity Magnitude	1.5876×10^{-7}	Rotational Process Noise - 1.3008×10^{-7}	Star Camera Noise - 6.3519×10^{-8}	Accelerometer Position - 4.2393×10^{-8}	rad/s

to the values given in the High Cost column of Tables 5, 6 (except the star camera noise is set equal to 10^{-5} rad), and 7. Results are generated by setting the parameters as per the values given in Tables 2, 3, and 8.

First, the results are presented for three accelerometers with initial 1σ error on spacecraft position, velocity, attitude, and angular velocity set equal to the values given in Table 3, accelerometer parameters are set as per Table 5, and the time constants are set as per Value 1 in Table 4.

Plots for the true navigation error 1σ standard deviation of all states, for the non-rotating inertially fixed spacecraft, show convergence to a steady-state value. However, the estimates for the accelerometer states do not converge to a steady-state value, especially accelerometer misalignment. One of the reasons for poor estimation of accelerometer states could be weak observability of these states. The error budget results for accelerometer states also reflect this, because the major source of error is the accelerometer error.

Error budget results are summarized in Table 11. Note that the total steady-state true navigation error is the RSS of all the error sources.

Plots for the true navigation error 1σ standard deviation of all states, for the rotating Nadir pointing spacecraft, show convergence to a steady-state value. However, the estimates for accelerometer states do not converge to a steady-state value, especially accelerometer misalignment. One of the reasons for poor estimation of accelerometer states is suspected to be weak observability of these states. The error budget results for accelerometer states also reflect this, and the major source of error is accelerometer error.

Error budget results are summarized in Table 12. Note that the total steady-state true navigation error is the RSS of all the error sources.

The results in Table 12 show that the estimates for the spacecraft position, velocity, attitude, angular velocity, and atmospheric parameter states improve (by about 8% in position and 40% in attitude) for the rotating spacecraft in comparison to that for the non-rotating spacecraft. Whereas, the estimates for spacecraft's center of mass position are marginally better for the non-rotating spacecraft. Estimates for accelerometer states show no change for the rotating spacecraft.

TABLE 12 Error budget of the maximum steady-state true navigation error 1σ std. deviation. For a rotating s/c in Polar LEO orbit, with 3 accel., 0.5 m baseline length, large time constant, & high cost model

State name	Total steady-state true navigation error 1σ	Error source 1	Error source 2	Error source 3	Units
Spacecraft Position Magnitude	77.54	Accelerometer Error - 69.63	Accelerometer Position - 28.61	Star Camera Noise - 11.69	m
Spacecraft Velocity Magnitude	0.08	Accelerometer Error - 0.07	Accelerometer Position - 0.03	Star Camera Noise - 0.01	m/s
Spacecraft Attitude Magnitude	6.0128×10^{-6}	Star Camera Noise - 5.0169×10^{-6}	Accelerometer Error - 2.5929×10^{-6}	Accelerometer Position - 1.7653×10^{-6}	rad
Spacecraft Angular Velocity Magnitude	6.3451×10^{-8}	Rotational Process Noise - 5.5115×10^{-8}	Accelerometer Error - 2.0514×10^{-8}	Accelerometer Position - 1.7138×10^{-8}	rad/s

Next, results are generated for moderate and low sensor grade for Polar LEO orbit. The filter performance is found to degrade and is similar to that for corresponding scenarios in LEO 50-degree inclination orbit. The reader is encouraged to please refer to these results in the dissertation by Bhatia (2019).

The above results are also repeated for the different number of accelerometers, different initial conditions, different time constants on atmospheric parameters, and different baseline length. Filter performance improves when the number of onboard accelerometers is increased. Filter performance is also better for the 1-m baseline length accelerometer configuration in comparison to that for the 0.5-m baseline length accelerometer configuration. These results are documented and discussed in detail by Bhatia (2019).

9 | CONCLUSION

LinCov results for a spacecraft in a LEO (50-degree inclination) and a polar LEO orbit have been presented, analyzed, and discussed in detail. Key contributions from this study are noted to be the development of the mathematical measurement model of electrostatic accelerometers, observability analysis for the autonomous navigation system, and the error budget results for a spacecraft in LEO regime.

An extensive detail about the existing technology and literature background of gravity gradiometry and spacecraft navigation has been discussed. Detailed problem setup and LinCov tool development has been presented along with the mathematical model for measurements and state dynamics. Observability analysis was conducted and the results were presented, so as to corroborate the idea of autonomous orbital navigation with advanced accelerometers.

Observability of spacecraft position, velocity, and attitude was proven for a configuration of three three-axis accelerometers. Feasibility of autonomous orbital navigation was established.

Error budget analysis for a non-rotating and a rotating spacecraft, in a low Earth orbit (50-degree inclination) and polar low Earth orbit, was conducted and results were documented.

Results were analyzed for three different sensor grades, and it was shown that the performance of the high sensor grade and precise system model satisfies the requirements for autonomous orbital navigation. Additionally, filter performance was shown to improve when the number of onboard accelerometers is increased. Filter performance was shown to be better for the 1-m baseline length accelerometer configuration in comparison to that for the 0.5-m baseline length accelerometer configuration. It has also been noted that the estimation of accelerometer scale-factor and misalignment is poor for all the scenarios.

Further, the major source of error for most of the scenarios has been sensor errors (like accelerometer error, accelerometer position uncertainty, or star camera noise). This is an important result as it highlights the sensor specifications to be improved so as to reduce the final navigation error.

This research highlighted the ultra-precise sensitivity requirements needed to generate accelerometer measurements and navigate autonomously in space.

In summary, the objective of the research, as stated earlier, has been accomplished.

The objective of this research is to use the Linear Covariance theory to investigate the feasibility and sensitivity requirements for an autonomous orbit determination using advanced accelerometer measurements and onboard gravity field maps for different sensor and orbit configurations.

10 | FUTURE WORK

This research presented an idea and a feasibility study along with the sensitivity requirements for developing an autonomous orbital navigation system based on ultra-precise accelerometers. To extend this idea of developing an autonomous orbital navigation system into reality, a detailed analysis and intensive study of the hardware of these ultra-precise sensors is needed.

Results presented in this study can be used to perform a detailed analysis by expanding the number of parameters and including uncertainties in the gravity field model and Earth model. Further, a suite of sensors can be included and different permutations can be tested accordingly.

A Monte Carlo analysis can be conducted, and an analysis may be performed in order to test and validate the linearized models. Different types of gravity models can be studied, and an effort may be made towards determining a computationally efficient method to store high-fidelity gravity maps onboard.

ORCID

Rachit Bhatia https://orcid.org/0000-0001-8869-5801

REFERENCES

Argentiero, P., & Garza-Robles, R. (1976). *A spacecraft-borne gradiometer mission analysis* (NASA TN D-8287). National Aeronautics and Space Administration.

Bhatia, R., & Geller, D. K. (2017, April). Autonomous navigation using gravity gradient measurements. *9th IAASS (International Association for the Advancement of Space Safety) Conference*, Toulouse, France.

Bhatia, R., & Geller, D. K. (2018, February). RAON: Revolution in autonomous orbital navigation. *41st American Astronomical Society (AAS) Guidance, Navigation, & Controls (GN&C) Conference*, Breckenridge, CO.

Bhatia, R. (2019). *Revolution in Autonomous Orbital Navigation (RAON)* (Doctoral dissertation, Utah State University). https://digitalcommons.usu.edu/etd/7676/

Bobojć, A., & Drożyner, A. (2003). Satellite orbit determination using satellite gravity gradiometry observations in GOCE mission perspective. *Advances in Geosciences*, *1*, 109–112.

Bond, V. R., & Allman, M. C. (1996). *Modern astrodynamics: Fundamentals and perturbation methods*. Cambridge Studies in Advanced Mathematics, Princeton University Press.

Cesare, S. (2002). *Performance requirements and budgets for the gradiometric mission* (Technical note GOC-TN-AI-0027). Alenia Spazio.

Chen, P., Sun, X., & Han, C. (2015). Gravity gradient tensor eigendecomposition for spacecraft positioning. *Journal of Guidance, Control, and Dynamics*, *38*(11), 2200–2206. https://doi.org/10.2514/1.G001195

Christensen, R. S. (2013). *Linear covariance analysis for gimbaled pointing systems*. Utah State University.

Christensen, R. S., & Geller, D. (2014). Linear covariance techniques for closed-loop guidance navigation and control system design and analysis. *Proceedings of the Institution of Mechanical Engineers, Part G: Journal of Aerospace Engineering*, *228*(1), 44–65. https://doi.org/10.1177/0954410012467717

DiFrancesco, D., Grierson, A., Kaputa, D., & Meyer, T. (2009a). Gravity gradiometer systems–advances and challenges. *Geophysical Prospecting*, *57*(4), 615–623. https://doi.org/10.1111/j.1365-2478.2008.00764.x

DiFrancesco, D., Meyer, T., Christensen, A., & FitzGerald, D. (2009b, September). Gravity gradiometry–today and tomorrow. *11th SAGA Biennial Technical Meeting and Exhibition*, Swaziland, South Africa, 80–83. https://doi.org/10.3997/2214-4609-pdb.241.difrancesco_paper1

Geller, D. K. (2006). Linear covariance techniques for orbital rendezvous analysis and autonomous onboard mission planning. *Journal of Guidance, Control, and Dynamics*, *29*(6), 1404–1414. https://doi.org/10.2514/1.19447

Geller, D. K., & Bhatia, R. (2018, August). Orbit and attitude observability using accelerometer measurements. *2018 AAS/AIAA Astrodynamics Specialist Conference*, Snowbird, UT.

Gill Oliver, M. E., & Montenbruck, O. (2012). *Satellite orbits*. Springer.

Gray, S. D., Parmentola, J. A., & LeSchack, R. (1995). Estimating the weight of very heavy objects with a gravity gradiometer. *Journal of Physics D: Applied Physics*, *28*(11), 2378. https://doi.org/10.1088/0022-3727/28/11/024

Hofmann-Wellenhof, B., & Moritz, H. (2006). *Physical geodesy*. Springer Science & Business Media.

Jekeli, C. (1993). A review of gravity gradiometer survey system data analyses. *Geophysics*, *58*(4), 508–514. https://doi.org/10.1190/1.1443433

Jekeli, C. (2011). Gravity, gradiometry. In H. K. Gupta (Ed.), *Encyclopedia of solid earth geophysics* (pp. 547–561). Springer.

Kasevich, M. (2006). *Navigation, gravitation and cosmology with cold atom sensors*. Stanford Center for Position, Navigation and Time.

Kasevich, M. (2007). *Cold atom navigation sensors*. Stanford Center for Position, Navigation and Time.

Király, P. (1996, July). Eötvös and STEP. *Proceedings of the STEP (Satellite Test of the Equivalence Principle) Symposium*, Noordwijk, The Netherlands, 399–406.

Lefferts, E. J., Markley, F. L., & Shuster, M. D. (1982). Kalman filtering for spacecraft attitude estimation. *Journal of Guidance, Control, and Dynamics*, *5*(5), 417–429. https://doi.org/10.2514/3.56190

Markley, F. L., & Crassidis, J. L. (2014). *Fundamentals of spacecraft attitude determination and control*. Space Technology Library Springer.

Paik, H. J., & Morgan, S. H. (1993). Superconducting gravity gradiometer mission. In M. Demianski and C. W. F. Everitt (Eds.), *Relativistic gravitational experiments in space*. World Scientific.

Pedersen, L. B., & Rasmussen, T. M. (1990). The gradient tensor of potential field anomalies: Some implications on data collection and data processing of maps. *Geophysics*, *55*(12), 1558–1566. https://doi.org/10.1190/1.1442807

Pei, C., Tengda, S., & Xiucong, S. (2017). Autonomous orbit determination using epoch-differenced gravity gradients and starlight refraction. *Chinese Journal of Aeronautics*, *30*(5), 1740–1749. https://doi.org/10.1016/j.cja.2017.07.003

Pittelkau, M. E. (2003). Rotation vector in attitude estimation. *Journal of Guidance, Control, and Dynamics*, *26*(6), 855–860. https://doi.org/10.2514/2.6929

Richeson, J. A. (2008). *Gravity gradiometer aided inertial navigation within non-GNSS environments* (Doctoral dissertation, University of Maryland). https://drum.lib.umd.edu/handle/1903/7852

Roithmayr, C. M. (1990). Contribution of zonal harmonics to gravitational moment. *Journal of Guidance, Control, and Dynamics*, *14*(1). https://doi.org/10.2514/3.20626

Roithmayr, C. M. (2004). *Contributions of spherical harmonics to magnetic and gravitational fields* (NASA/TM–2004-213007). National Aeronautics and Space Administration.

Roithmayr, C. M. (2019). Contributions of Spherical Harmonics to Gravitational Moment. *AIAA Journal*, 1–10. https://doi.org/10.2514/1.J057227

Silvestrin, P., Aguirre, M., Massotti, L., Leone, B., Cesare, S., Kern, M, & Haagmans, R. (2012). *The future of the satellite gravimetry after the GOCE mission* (pp. 223–230). Springer.

Sonnabend, D., & Born, G. H. (1994). *Measuring attitude with a gradiometer* (N94- 35630). National Aeronautics and Space Administration.

Sun, X., Chen, P., Macabiau, C., & Han, C. (2016a). Autonomous orbit determination via kalman filtering of gravity gradients. *IEEE Transactions on Aerospace and Electronic Systems*, *52*(5), 2436–2451. https://doi.org/10.1109/TAES.2016.150387

Sun, X., Chen, P., Macabiau, C., & Han, C. (2016b). Low-earth orbit determination from gravity gradient measurements. *Acta Astronautica*, *123*, 350–362. https://doi.org/10.1016/j.actaastro.2016.03.012

Takahashi, Y., Busch Michael, W., & Scheeres, D. J. (2013). Spin state and moment of inertia characterization of 4179 Toutatis. *The Astronomical Journal*, *146*(4), 95. https://doi.org/10.1088/0004-6256/146/4/95

Vallado, D. A. (2001). *Fundamentals of astrodynamics and applications*. Springer Science & Business Media.

Veryaskin, A. V. (2018). *Gravity, magnetic and electromagnetic gradiometry* (pp. 2053–2571). Morgan & Claypool Publishers.

Wells, W. C. (1984). *Spaceborne gravity gradiometers* (Publication 2305). National Aeronautics and Space Administration.

Wertz, J. R. (1978). *Spacecraft attitude determination and control*. Astrophysics and Space Science Library Springer Netherlands.

Zhu, Z., Zhou, Z. B., Cai, L., Bai, Y. Z., & Luo, J. (2013). Electrostatic gravity gradiometer design for the future mission. *Advances in Space Research*, *51*(12), 2269–2276. https://doi.org/10.1016/j.asr.2013.01.031

How to cite this article: Bhatia R, Geller D. Sensitivity Analysis of Precision Inertial Sensor-based Navigation System (SAPIENS). *NAVIGATION*. 2020;67:795–822. https://doi.org/10.1002/navi.397

APPENDIX A

This appendix highlights some additional partial derivatives.

Partial of gravitational acceleration with respect to the spacecraft position is given as follows:

$$\left.\frac{\partial \mathbf{g}_E^I\left(\mathbf{r}_{CM/E}^I\right)}{\partial \mathbf{r}_{CM/E}^I}\right|_{\bar{\mathbf{x}}} = \nabla \mathbf{g}_E^I\left(\bar{\mathbf{r}}_{CM/E}^I\right). \tag{A.1}$$

Partial of acceleration due to atmospheric drag with respect to the spacecraft position is given as follows:

$$\left.\frac{\partial \mathbf{a}_{aero}^I}{\partial \mathbf{r}_{CM/E}^I}\right|_{\bar{\mathbf{x}}} = \frac{1}{2}\bar{\rho}_r e^{\frac{-\left(\left\|\bar{\mathbf{r}}_{CM/E}^I\right\|-h_{ref}\right)}{\bar{h}_s}} \bar{\beta}\left\|\bar{\mathbf{v}}_{CM/E}^I\right\|\bar{\mathbf{v}}_{CM/E}^I \frac{\hat{\mathbf{i}}_{\bar{\mathbf{r}}_{CM/E}^I}^T}{\bar{h}_s}. \tag{A.2}$$

Partial of acceleration due to atmospheric drag with respect to the spacecraft velocity is given as follows:

$$\left.\frac{\partial \mathbf{a}_{aero}^I}{\partial \mathbf{v}_{CM/E}^I}\right|_{\bar{\mathbf{x}}} = -\frac{1}{2}\bar{\rho}_r e^{\frac{-\left(\left\|\bar{\mathbf{r}}_{CM/E}^I\right\|-h_{ref}\right)}{\bar{h}_s}} \bar{\beta}\left(\bar{\mathbf{v}}_{CM/E}^I \hat{\mathbf{i}}_{\bar{\mathbf{v}}_{CM/E}^I}^T + \left\|\bar{\mathbf{v}}_{CM/E}^I\right\| I_{3\times 3}\right). \tag{A.3}$$

Partial of acceleration due to atmospheric drag with respect to the spacecraft ballistic coefficient is given as follows:

$$\left.\frac{\partial \mathbf{a}_{aero}^I}{\partial \beta}\right|_{\bar{\mathbf{x}}} = -\frac{1}{2}\bar{\rho}_r e^{\frac{-\left(\left\|\bar{\mathbf{r}}_{CM/E}^I\right\|-h_{ref}\right)}{\bar{h}_s}} \left\|\bar{\mathbf{v}}_{CM/E}^I\right\|\bar{\mathbf{v}}_{CM/E}^I. \tag{A.4}$$

Partial of acceleration due to atmospheric drag with respect to the reference atmospheric density is given as follows:

$$\left.\frac{\partial \mathbf{a}_{aero}^I}{\partial \rho_r}\right|_{\bar{\mathbf{x}}} = -\frac{1}{2} e^{\frac{-\left(\left\|\bar{\mathbf{r}}_{CM/E}^I\right\|-h_{ref}\right)}{\bar{h}_s}} \bar{\beta}\left\|\bar{\mathbf{v}}_{CM/E}^I\right\|\bar{\mathbf{v}}_{CM/E}^I. \tag{A.5}$$

Partial of acceleration due to atmospheric drag with respect to the scale height is given as follows:

$$\left.\frac{\partial \mathbf{a}_{aero}^I}{\partial h_s}\right|_{\bar{\mathbf{x}}} = C_{alt}\bar{\rho}_r e^{\frac{-\left(\left\|\bar{\mathbf{r}}_{CM/E}^I\right\|-h_{ref}\right)}{\bar{h}_s}} \bar{\beta}\left\|\bar{\mathbf{v}}_{CM/E}^I\right\|\bar{\mathbf{v}}_{CM/E}^I, \tag{A.6}$$

where C_{alt} is a constant given as

$$C_{alt} = -\frac{\left(\left\|\bar{\mathbf{r}}_{CM/E}^I\right\| - h_{ref}\right)}{2\bar{h}_s^2}. \tag{A.7}$$

Solar radiation pressure perturbation partial with respect to the spacecraft position in the inertial frame is

computed as follows:

$$\left.\frac{\partial \mathbf{a}^I_{SRP}}{\partial \mathbf{r}^I_{CM/E}}\right|_{\bar{\mathbf{x}}} = \frac{F_e}{c}\left[\frac{3}{r_{sc}\rho_{sc}}\right]\left[\frac{1}{4}+\frac{1}{9}d_r\right]\left[\frac{\partial\left(\frac{\mathbf{r}^I_{CM/E}-\boldsymbol{\rho}_{Sun}}{\left\|\mathbf{r}^I_{CM/E}-\boldsymbol{\rho}_{Sun}\right\|}\right)}{\partial \mathbf{r}^I_{CM/E}}\right]_{\bar{\mathbf{x}}} \tag{A.8}$$

$$\left.\frac{\partial \mathbf{a}^I_{SRP}}{\partial \mathbf{r}^I_{CM/E}}\right|_{\bar{\mathbf{x}}} = \frac{F_e}{c\left\|\bar{\mathbf{r}}^I_{CM/E}-\boldsymbol{\rho}_{Sun}\right\|}\left[\frac{3}{r_{sc}\rho_{sc}}\right]\left[\frac{1}{4}+\frac{1}{9}d_r\right]\left[I_{3\times3} - \hat{\mathbf{i}}^I_{CM/Sun}\left(\hat{\mathbf{i}}^I_{CM/Sun}\right)^T\right], \tag{A.9}$$

where $\hat{\mathbf{i}}^I_{CM/Sun}$ is the unit vector defined as

$$\hat{\mathbf{i}}^I_{CM/Sun} = \frac{\bar{\mathbf{r}}^I_{CM/E}-\boldsymbol{\rho}_{Sun}}{\left\|\bar{\mathbf{r}}^I_{CM/E}-\boldsymbol{\rho}_{Sun}\right\|}. \tag{A.10}$$

Third-body perturbation partial with respect to the spacecraft position in the inertial frame is computed as follows:

$$\left.\frac{\partial \mathbf{a}^I_{3rd}}{\partial \mathbf{r}^I_{CM/E}}\right|_{\bar{\mathbf{x}}} = \left.\frac{-Gm_{3rd}\partial\left(\frac{\mathbf{r}^I_{CM/E}-\boldsymbol{\rho}_{3rd}}{\left\|\mathbf{r}^I_{CM/E}-\boldsymbol{\rho}_{3rd}\right\|^3}+\frac{\boldsymbol{\rho}_{3rd}}{\|\boldsymbol{\rho}_{3rd}\|^3}\right)}{\partial \mathbf{r}^I_{CM/E}}\right|_{\bar{\mathbf{x}}} \tag{A.11}$$

$$\left.\frac{\partial \mathbf{a}^I_{3rd}}{\partial \mathbf{r}^I_{CM/E}}\right|_{\bar{\mathbf{x}}} = \frac{-Gm_{3rd}}{\left\|\bar{\mathbf{r}}^I_{CM/E}-\boldsymbol{\rho}_{3rd}\right\|^3}\left[I_{3\times3} - 3\hat{\mathbf{i}}^I_{CM/3rd}\left(\hat{\mathbf{i}}^I_{CM/3rd}\right)^T\right], \tag{A.12}$$

where m_{3rd} is the mass of the third body (Sun, Moon, etc.), and $\hat{\mathbf{i}}^I_{CM/3rd}$ is the unit vector defined as

$$\hat{\mathbf{i}}^I_{CM/3rd} = \frac{\bar{\mathbf{r}}^I_{CM/E}-\boldsymbol{\rho}_{3rd}}{\left\|\bar{\mathbf{r}}^I_{CM/E}-\boldsymbol{\rho}_{3rd}\right\|}. \tag{A.13}$$

Gravity gradient torque partial with respect to the spacecraft position is computed as follows:

$$\left.\frac{\partial M_{gg}}{\partial \mathbf{r}^I_{CM/E}}\right|_{\bar{\mathbf{x}}} = \left.\frac{\partial\left\{\frac{3\mu}{\left\|\mathbf{r}^B_{CM/E}\right\|^5}\left(\mathbf{r}^B_{CM/E}\times\left[J\mathbf{r}^B_{CM/E}\right]\right)\right\}}{\partial \mathbf{r}^I_{CM/E}}\right|_{\bar{\mathbf{x}}} \tag{A.14}$$

$$\left.\frac{\partial M_{gg}}{\partial \mathbf{r}^I_{CM/E}}\right|_{\bar{\mathbf{x}}} = 3\mu\left[\mathbf{r}^B_{CM/E} \times\left(J\mathbf{r}^B_{CM/E}\right)\right]\frac{\partial\left(\frac{1}{\left\|\mathbf{r}^B_{CM/E}\right\|^5}\right)}{\partial\left\|\mathbf{r}^B_{CM/E}\right\|}\frac{\partial\left\|\mathbf{r}^B_{CM/E}\right\|}{\partial \mathbf{r}^B_{CM/E}}\frac{\partial \mathbf{r}^B_{CM/E}}{\partial \mathbf{r}^I_{CM/E}}\Bigg|_{\bar{\mathbf{x}}} + \left.\frac{(-3\mu)\left[\left(J\bar{\mathbf{r}}^B_{CM/E}\right)\times\right]}{\left\|\mathbf{r}^B_{CM/E}\right\|^5}\frac{\partial \mathbf{r}^B_{CM/E}}{\partial \mathbf{r}^B_{CM/E}}\frac{\partial \mathbf{r}^B_{CM/E}}{\partial \mathbf{r}^I_{CM/E}}\right|_{\bar{\mathbf{x}}} + \left.\frac{3\mu\left[\bar{\mathbf{r}}^B_{CM/E}\times\right]J}{\left\|\mathbf{r}^B_{CM/E}\right\|^5}\frac{\partial \mathbf{r}^B_{CM/E}}{\partial \mathbf{r}^B_{CM/E}}\frac{\partial \mathbf{r}^B_{CM/E}}{\partial \mathbf{r}^I_{CM/E}}\right|_{\bar{\mathbf{x}}} \tag{A.15}$$

$$\left.\frac{\partial M_{gg}}{\partial \mathbf{r}^I_{CM/E}}\right|_{\bar{\mathbf{x}}} = \frac{-3\mu}{\left\|\bar{\mathbf{r}}^B_{CM/E}\right\|^5}\left\{\frac{5\left[\bar{\mathbf{r}}^B_{CM/E}\times\left(J\bar{\mathbf{r}}^B_{CM/E}\right)\right]\hat{\mathbf{i}}^T_{\bar{\mathbf{r}}^B_{CM/E}}}{\left\|\bar{\mathbf{r}}^B_{CM/E}\right\|} + \left[\left(J\bar{\mathbf{r}}^B_{CM/E}\right)\times\right] - \left[\bar{\mathbf{r}}^B_{CM/E}\times\right]J\right\}T_{I\to B}. \tag{A.16}$$

Gravity gradient torque partial with respect to the rotation vector is computed as follows:

$$\left.\frac{\partial M_{gg}}{\partial \theta}\right|_{\bar{\mathbf{x}}} = \frac{-3\mu}{\left\|\mathbf{r}^B_{CM/E}\right\|^5}\left\{\left[\left(J\bar{\mathbf{r}}^B_{CM/E}\right)\times\right] - \left[\bar{\mathbf{r}}^B_{CM/E}\times\right]J\right\}\left[\bar{\mathbf{r}}^B_{CM/E}\times\right]. \tag{A.17}$$

Partial of accelerometer measurement with respect to the spacecraft rotation vector is given as follows:

$$\left.\frac{\partial \boldsymbol{a}^B_{d_i}}{\partial \theta}\right|_{\bar{\mathbf{x}}} = \left[\left\{T_{I\to\bar{B}}(\bar{\theta})\bar{\mathbf{a}}^I_{d_i}(\bar{\theta})\right\}\times\right] + T_{I\to\bar{B}}(\bar{\theta})\nabla\bar{\boldsymbol{g}}^I\left(\bar{\boldsymbol{r}}^I_{a_i/E}\right)T^T_{I\to\bar{B}}(\bar{\theta})\left[\bar{\mathbf{r}}^B_{a_i/CM}\times\right]. \tag{A.18}$$

Partial of accelerometer measurement with respect to the spacecraft angular velocity is given as follows:

$$\left.\frac{\partial \mathbf{a}^I_{d_i}}{\partial \boldsymbol{\omega}^B_{B/I}}\right|_{\bar{\mathbf{x}}} = T_{BI}\left.\frac{\partial\left[\boldsymbol{\omega}^B_{B/I}\times\left(\boldsymbol{\omega}^B_{B/I}\times\left(\mathbf{r}^B_{a_i/O}-\mathbf{r}^B_{CM/O}\right)\right)\right]}{\partial \boldsymbol{\omega}^B_{B/I}}\right|_{\bar{\mathbf{x}}} \tag{A.19}$$

$$\left.\frac{\partial \mathbf{a}^I_{d_i}}{\partial \boldsymbol{\omega}^B_{B/I}}\right|_{\bar{\mathbf{x}}} = -T_{BI}\left[\left.\frac{\partial\left\{\boldsymbol{\omega}^B_{B/I}\times\left(\left[\mathbf{r}^B_{a_i/O}-\mathbf{r}^B_{CM/O}\right]\times\boldsymbol{\omega}^B_{B/I}\right)\right\}}{\partial\boldsymbol{\omega}^B_{B/I}}\right|_{\bar{\mathbf{x}}} + \left.\frac{\partial\left\{\left(\boldsymbol{\omega}^B_{B/I}\times\left[\mathbf{r}^B_{a_i/O}-\mathbf{r}^B_{CM/O}\right]\right)\times\boldsymbol{\omega}^B_{B/I}\right\}}{\partial\boldsymbol{\omega}^B_{B/I}}\right|_{\bar{\mathbf{x}}}\right] \tag{A.20}$$

$$\left.\frac{\partial \mathbf{a}^I_{d_i}}{\partial \boldsymbol{\omega}^B_{B/I}}\right|_{\bar{\mathbf{x}}} = -T_{BI}\left\{\left[\left(\bar{\boldsymbol{\omega}}^B_{B/I}\times\left[\bar{\mathbf{r}}^B_{a_i/O}-\bar{\mathbf{r}}^B_{CM/O}\right]\right)\times\right] + \left[\bar{\boldsymbol{\omega}}^B_{B/I}\times\right]\left[\left(\bar{\mathbf{r}}^B_{a_i/O}-\bar{\mathbf{r}}^B_{CM/O}\right)\times\right]\right\}, \tag{A.21}$$

where T_{BI} is the transformation from SBRF to IRF, given as

$$T_{BI} = T_{B\to I}(\mathbf{q}_{B\to I}). \tag{A.22}$$

Partial of accelerometer measurement with respect to the spacecraft's center of mass position, in spacecraft body-fixed frame and with respect to the origin of spacecraft body-fixed frame, is given as

$$\left.\frac{\partial \mathbf{a}^I_{d_i}}{\partial \mathbf{r}^B_{CM/O}}\right|_{\bar{\mathbf{x}}} = -\left.\frac{\partial\left\{\mathbf{g}^I\left(\mathbf{r}^I_{CM/E}+T_{BI}\left[\mathbf{r}^B_{a_i/O}-\mathbf{r}^B_{CM/O}\right]\right)\right\}}{\partial\mathbf{r}^B_{CM/O}}\right|_{\bar{\mathbf{x}}} + T_{BI}\left.\frac{\partial\left\{\boldsymbol{\omega}^B_{B/I}\times\left(\boldsymbol{\omega}^B_{B/I}\times\left[\mathbf{r}^B_{a_i/O}-\mathbf{r}^B_{CM/O}\right]\right)\right\}}{\partial\mathbf{r}^B_{CM/O}}\right|_{\bar{\mathbf{x}}} \tag{A.23}$$

$$\left.\frac{\partial \mathbf{a}^I_{d_i}}{\partial \mathbf{r}^B_{CM/O}}\right|_{\bar{\mathbf{x}}} = -\left.\frac{\partial\left\{\mathbf{g}^I\left(\bar{\boldsymbol{r}}^I_{a_i/E}\right)\right\}}{\partial\mathbf{r}^I_{a_i/E}}\right|_{\bar{\mathbf{x}}}\left.\frac{\partial\left(\mathbf{r}^I_{a_i/E}\right)}{\partial\mathbf{r}^B_{CM/O}}\right|_{\bar{\mathbf{x}}} + T_{BI}\left(\left.\frac{\partial\left\{\left[\bar{\boldsymbol{\omega}}^B_{B/I}\times\right]\left[\bar{\boldsymbol{\omega}}^B_{B/I}\times\right]\left[\mathbf{r}^B_{a_i/O}-\mathbf{r}^B_{CM/O}\right]\right\}}{\partial\mathbf{r}^B_{CM/O}}\right|_{\bar{\mathbf{x}}}\right) \tag{A.24}$$

$$\left.\frac{\partial \mathbf{a}^I_{d_i}}{\partial \mathbf{r}^B_{CM/O}}\right|_{\bar{\mathbf{x}}} = \nabla\bar{\boldsymbol{g}}^I\left(\bar{\boldsymbol{r}}^I_{a_i/E}\right)T_{BI} - T_{BI}\left(\left[\bar{\boldsymbol{\omega}}^B_{B/I}\times\right]\left[\bar{\boldsymbol{\omega}}^B_{B/I}\times\right]\right). \tag{A.25}$$

Partial of accelerometer measurement with respect to the i^{th} accelerometer position, in spacecraft body-fixed frame and with respect to the origin of the spacecraft body-fixed frame ($\mathbf{r}^B_{a_i/O}$), is given as

$$\left.\frac{\partial \mathbf{a}^I_{d_i}}{\partial \mathbf{r}^B_{a_i/O}}\right|_{\bar{\mathbf{x}}} = -\left.\frac{\partial\left\{\mathbf{g}^I\left(\mathbf{r}^I_{CM/E}+T_{BI}\left[\mathbf{r}^B_{a_i/O}-\mathbf{r}^B_{CM/O}\right]\right)\right\}}{\partial\mathbf{r}^B_{a_i/O}}\right|_{\bar{\mathbf{x}}} + T_{BI}\left.\frac{\partial\left\{\boldsymbol{\omega}^B_{B/I}\times\left(\boldsymbol{\omega}^B_{B/I}\times\left[\mathbf{r}^B_{a_i/O}-\mathbf{r}^B_{CM/O}\right]\right)\right\}}{\partial\mathbf{r}^B_{a_i/O}}\right|_{\bar{\mathbf{x}}} \tag{A.26}$$

$$\left.\frac{\partial \mathbf{a}^I_{d_i}}{\partial \mathbf{r}^B_{a_i/O}}\right|_{\bar{\mathbf{x}}} = -\left.\frac{\partial\left\{\mathbf{g}^I\left(\bar{\boldsymbol{r}}^I_{a_i/E}\right)\right\}}{\partial\mathbf{r}^I_{a_i/E}}\right|_{\bar{\mathbf{x}}}\left.\frac{\partial\left(\mathbf{r}^I_{a_i/E}\right)}{\partial\mathbf{r}^B_{a_i/O}}\right|_{\bar{\mathbf{x}}} + T_{BI}\left(\left.\frac{\partial\left\{\left[\bar{\boldsymbol{\omega}}^B_{B/I}\times\right]\left[\bar{\boldsymbol{\omega}}^B_{B/I}\times\right]\left[\mathbf{r}^B_{a_i/O}-\mathbf{r}^B_{CM/O}\right]\right\}}{\partial\mathbf{r}^B_{a_i/O}}\right|_{\bar{\mathbf{x}}}\right) \tag{A.27}$$

$$\left.\frac{\partial \mathbf{a}^I_{d_i}}{\partial \mathbf{r}^B_{a_i/O}}\right|_{\bar{\mathbf{x}}} = -\nabla\bar{\boldsymbol{g}}^I\left(\bar{\boldsymbol{r}}^I_{a_i/E}\right)T_{BI} + T_{BI}\left(\left[\bar{\boldsymbol{\omega}}^B_{B/I}\times\right]\left[\bar{\boldsymbol{\omega}}^B_{B/I}\times\right]\right). \tag{A.28}$$